Materials & Design 233 (2023) 112197

Contents lists available at ScienceDirect

Materials & Design

journal homepage: www.elsevier.com/locate/matdes

Experimental and numerical characterization of imperfect additively manufactured lattices based on triply periodic minimal surfaces

Fabian Günther [a,b,*], Stefan Pilz [c], Franz Hirsch [d], Markus Wagner [b], Markus Kästner [d,e,f], Annett Gebert [c], Martina Zimmermann [a,b]

[a] Institute of Materials Science, TU Dresden, Helmholtzstraße 7, 01069 Dresden, Germany
[b] Institute for Material and Beam Technology, Fraunhofer IWS, Winterbergstraße 28, 01277 Dresden, Germany
[c] Institute for Complex Materials, Leibniz IFW Dresden, Helmholtzstraße 20, 01069 Dresden, Germany
[d] Institute of Solid Mechanics, TU Dresden, George-Bähr-Straße 3c, 01069 Dresden, Germany
[e] Dresden Center for Fatigue and Reliability, DCFR, 01062 Dresden, Germany
[f] Dresden Center for Computational Materials Science, DCMS, 01062 Dresden, Germany

ARTICLE INFO

Keywords:
Lattice structures
Triply periodic minimal surfaces
Additive manufacturing
Imperfect lattices
Numerical reconstruction

ABSTRACT

Lattices based on triply periodic minimal surfaces (TPMS) are attracting increasing interest in seminal industries such as bone tissue engineering due to their excellent structure-property relationships. However, the potential can only be exploited if their structural integrity is ensured. This requires a fundamental understanding of the impact of imperfections that arise during additive manufacturing. Therefore, in the present study, the structure-property relationships of eight TPMS lattices, including their imperfections, are investigated experimentally and numerically. In particular, the focus is on biomimetic network TPMS lattices of the type Schoen I-WP and Gyroid, which are fabricated by laser powder bed fusion from the biocompatible alloy Ti-42Nb. The experimental studies include computed tomography measurements and compression tests. The results highlight the importance of process-related imperfections on the mechanical performance of TPMS lattices. In the numerical work, firstly the as-built morphology is artificially reconstructed before finite element analyses are performed. Here, the reconstruction procedure previously developed by the same authors is used and validated on a larger experimental matrix before more advanced calculations are conducted. Specifically, the reconstruction reduces the numerical overestimation of stiffness from up to 341% to a maximum of 26% and that of yield strength from 66% to 12%. Given a high simulation accuracy and flexibility, the presented procedure can become a key factor in the future design process of TPMS lattices.

1. Introduction

Lattice structures based on triply periodic minimal surfaces (TPMS) have emerged as an attractive option for various industrial applications. This is especially true for bone tissue engineering (BTE), in which implants are developed to replace or support injured bone [1–3]. The keen interest in TPMS based lattices is explained by the variety of exceptional properties, including high strength with low stiffness [4,5], good permeability [6,7] and the ability of functional grading [8,9]. In implant applications, this combination helps to reduce the risk of the stress-shielding effect and to support osseointegration while maintaining the required strength [10,11].

Due to the excellent biocompatibility and low Young's modulus, permanent implants are mostly made of titanium and its alloys. The current 'gold standard' is Ti-6Al-4V with a Young's modulus around 115 GPa, but the discrepancy with human bone with 0.1 - 20 GPa is still quite significant [12,13]. Therefore, recent work has focused on the development of low modulus beta-Ti alloys, such as Ti-42Nb [14]. The Young's modulus around 60 GPa helps in designing stiffness neutral implants providing proper bone stimulation. Simultaneously, the yield strength of up to 700 MPa permits the design of open-pore lattices that promote cell adhesion and proliferation [15,16]. Metal additive manufacturing (AM) enables the production of complex structures like TPMS lattices from such materials. Here, laser powder bed fusion (LPBF) is the most

* Corresponding author at: Institute of Materials Science, TU Dresden, Helmholtzstraße 7, 01069 Dresden, Germany.
E-mail address: fabian.guenther@tu-dresden.de (F. Günther).

https://doi.org/10.1016/j.matdes.2023.112197
Received 14 June 2023; Received in revised form 26 July 2023; Accepted 27 July 2023
Available online 9 August 2023

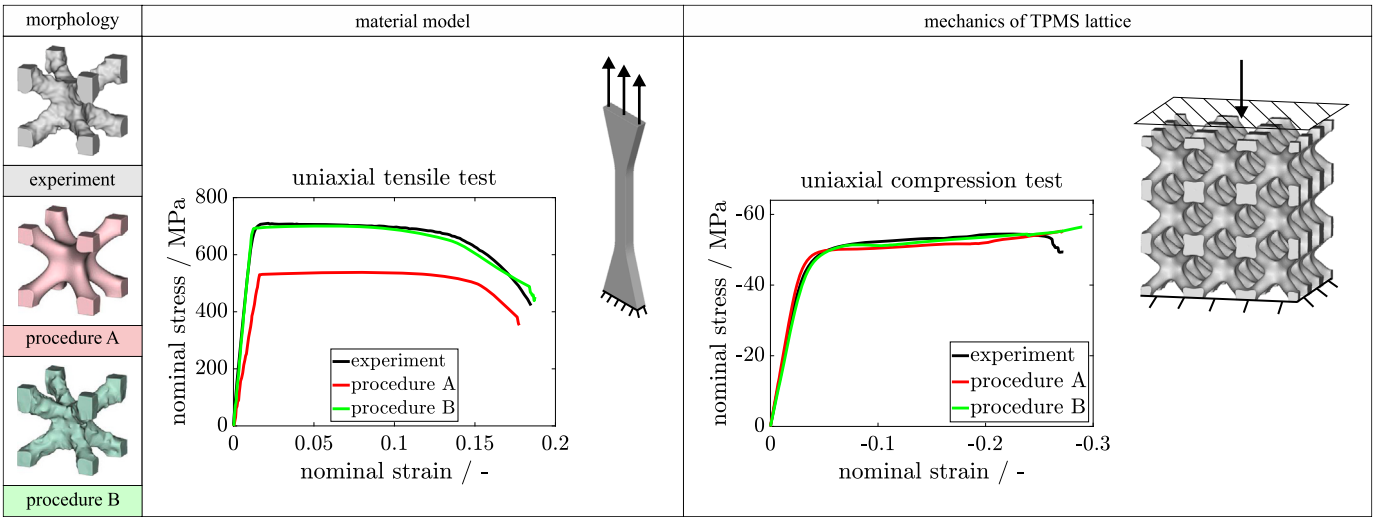

Fig. 1. Schematic representation of two numerical approaches for structure-property studies of imperfect lattices: procedure A uses the as-designed lattice morphology and an adapted material model to represent the mechanical behavior of the lattice; procedure B uses an as-built-like morphology derived from μ-CT data together with a material model obtained from bulk specimens. The latter is applied in this study, cf. Section 2.2.

widely used technology, given a minimum feature size of a few hundred micrometers [17,18].

TPMS based scaffolds for BTE have already been extensively fabricated using LPBF and experimentally characterized. Besides the convincing structure-property relationships [19–21] and the promising results for osseointegration performance [22–24], however, the impact of process-related imperfections became apparent. Here, imperfection refers to any target-actual deviation occurring during production. Due to their large surface area, TPMS lattices are comparatively difficult to manufacture and therefore prone to defects [17,25]. Usually, internal and external defects are distinguished: the first class concerns imperfections in the microstructure such as pores, whereas the second class includes all surface phenomena such as roughness and shape deviation [26–28].

Pore formation can be sensitively controlled by process parameter selection. Typically, material densities greater than 99.9% are achieved after parameter optimization [29]. Furthermore, the influence of internal imperfections can be significantly reduced by suitable post-treatment, such as hot isostatic pressing [13,30]. In contrast, external imperfections remain a major issue of LPBF processed structures: although surface roughness can be partially eliminated by etching [31] or sandblasting [32,33], the larger shape deviations can only be insufficiently avoided by process control or post-treatment. Due to the layer-by-layer manufacturing process and local overmelting, surface areas with more than 45° overhang are particularly predestined for such imperfections. Numerous quantitative data can be found in the literature depending on TPMS type, cell size and material. Accordingly, the excess material on overhanging surfaces amounts to 200 - 500 μm [34–37].

Since imperfections have a critical impact on the performance and failure of lattices, research aims at a deeper understanding of process-structure-property relationships. Besides process optimization and post-treatment [14,38], the question of structure-property relationships of imperfect lattices is the focus of interest. Here, finite element (FE) analysis plays an increasingly important role [39,40]. In order to realistically represent the mechanical behavior including the influence of imperfections, two primary procedures have emerged, both illustrated in **Fig. 1**.

Classically (procedure A), the models include the as-designed morphology [41,42]. By adjusting the material model, the mechanical behavior of a lattice can be retrospectively captured with this procedure. However, the morphological simplification in this backward procedure is accompanied by an unrealistic material model when tests on bulk specimens are considered. For this reason, an alternative forward approach (procedure B) has been developed, in which the morphology is artificially adjusted to the as-built state [43–46]. Typically, computed tomography (CT) scans form the basis for these reconstructions. The advantage of this procedure is that the material model can be derived from the tests on bulk specimens. Thus, the actual performance of a lattice can be predicted non-destructively based on material data and μ-CT data.

Recent work aims to exploit the systematic nature of imperfections in lattice structures. Specifically, the target-actual deviations found in μ-CT scans are no longer copied one-to-one. Instead, modeling routines are being developed that can artificially reproduce the essential features of the as-built morphology. Noteworthy are the studies by Lozanovski et al. [47–49], in which a reconstruction method for strut-based trusses was introduced. For TPMS lattices, the foundation in this branch of research was laid with our previous work [50], but the effectiveness has only been demonstrated on a single lattice so far.

This is where the present study comes in: by validating against a comprehensive experimental matrix, the numerical tool of reconstruction shall be unlocked for a wide range of users. In particular, the structure-property relationships of eight promising TPMS based bone substitutes made of LPBF processed Ti-42Nb are investigated experimentally and numerically. Firstly, the lattices are morphologically surveyed by μ-CT and mechanically characterized by uniaxial compression tests. Secondly, the as-built state of the lattices is artificially reconstructed and FE analyses are performed. Thirdly, further numerical investigations are carried out regarding the influence of cell size and the mechanical impact of different types of imperfections.

2. Methods

In this section, the experimental and numerical procedures are described. Section 2.1 includes experimental principles, including material, design, fabrication and testing. Subsequently, Section 2.2 outlines the reconstruction procedure of the imperfect TPMS lattices before Section 2.3 covers the FE modeling.

2.1. Experimental work

The specimens are based on the TPMS types Schoen I-WP and Gyroid in network configuration and have a volume fraction $\varphi = 0.25$. These lattices have proven to be particularly suitable candidates for BTE [51]. The lattices are obtained by the relation $\Phi + r = 0$, where Φ denotes the level set equation of a TPMS and r the level set constant controlling

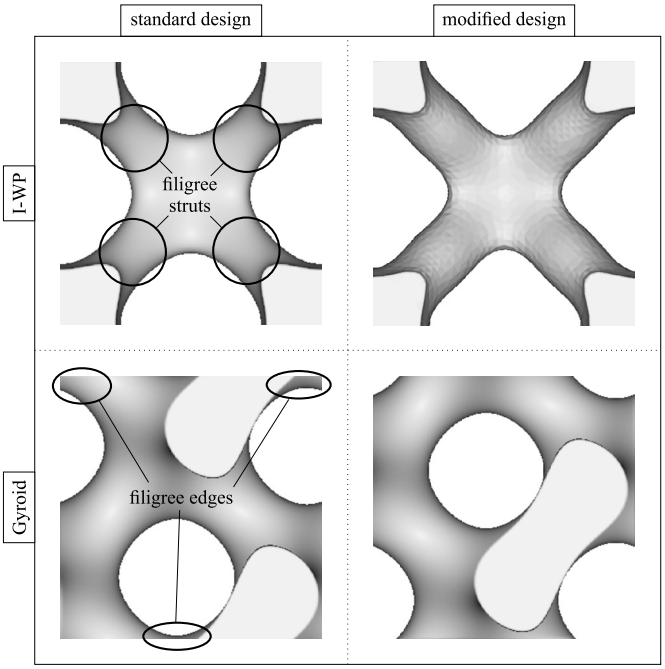

Fig. 2. Unit cells of the considered TPMS types I-WP and Gyroid in standard and modified design. For details on modeling, see [51].

Table 1
Considered TPMS based network lattices with 0.25 volume fraction.

notation	TPMS	cell number	cell size	design
2x2x2-I*-2	I-WP	2 x 2 x 2	2 mm	modified
2x2x2-I*-4	I-WP	2 x 2 x 2	4 mm	modified
2x2x2-G*-2	Gyroid	2 x 2 x 2	2 mm	modified
2x2x2-G*-4	Gyroid	2 x 2 x 2	4 mm	modified
3x3x3-I-2	I-WP	3 x 3 x 3	2 mm	standard
3x3x3-I*-2	I-WP	3 x 3 x 3	2 mm	modified
3x3x3-G-2	Gyroid	3 x 3 x 3	2 mm	standard
3x3x3-G*-2	Gyroid	3 x 3 x 3	2 mm	modified

the volume fraction. Besides the standard design, a modified design is investigated in each case, which is aimed at improving mechanical performance [52]: for the I-WP lattice, functional gradations are performed to thicken the strut centers relative to the nodes. For the Gyroid lattice, the design domain is selectively positioned to avoid filigree edges. The modeling of specimens and the generation of STL files is done with MATLAB software (MathWorks, USA). Further details on the implicit modeling can be found in [50,51]. The four unit cell designs are shown in **Fig. 2**. In order to investigate the influence of TPMS type, cell size and design modification, a total of eight different variants are considered. Their specifications and notations are listed in **Table 1**.

The specimens are fabricated from a Ti-42Nb alloy by LPBF. The prealloyed, gas-atomized Ti-42Nb powder is supplied by TANIOBIS GmbH (Germany). A SLM 280 Generation 2.0 dual-laser machine (SLM Solutions Group AG, Germany) equipped with an infrared laser source with a Gaussian beam profile and 80 µm beam size is used. Here, a laser power of 210 W, a scan speed of 1050 mm/s, a hatch distance of 100 µm, a layer thickness of 50 µm and a scan rotation of 67° are applied. The lattices are removed from the building plate by spark erosion and ground plane-parallel by hand, but otherwise not post-processed. Further details on manufacturing and material can be found in [14,50].

µ-CT measurements are performed using a GE Phoenix Nanotom M (Waygate Technologies, Germany) on one specimen of each of all specimen variants. Thus, the manufacturing quality is monitored, and the material density and the volume fraction are measured. 360° scans are obtained by taking 1000 absorption images with $t = 1250$ ms exposure time, $U = 130$ kV accelerating voltage and $I = 110$ µA current. The voxel size resolution is 5.2 - 8.6 µm depending on the unit cell size. For volume reconstruction and analysis, the software Phoenix datos|x 2.2 (Baker Hughes, USA) and VGSTUDIO max 2022.2 (Volume Graphics, Germany) are used. In addition, digital microscope images are acquired using a VHX7000 digital microscope (Keyence Deutschland GmbH, Germany).

Mechanical characterization consists of uniaxial quasi-static compression tests. A tension-compression module (Kammrath & Weiss GmbH, Germany) with a 10 kN load cell and a strain rate of $0.125\,\mathrm{min}^{-1}$ is used. The machine is equipped with plane-parallel stainless steel anvils for load transfer. To study the influence of the loading direction with respect to the build direction (BD), all specimen variants with 2 mm unit cells are tested parallel and perpendicular to the BD. The lattices with 4 mm cell size are tested parallel to the BD. During the tests, the force in the load cell and the crosshead travel of the testing machine are measured. Nominal strains are calculated by relating the displacement to the initial lattice height l and nominal stresses by relating the force to the initial cross-sectional area l^2. The effective compressive stiffness $\bar{E}$ in the elastic regime and the effective compressive yield strength $\bar{\sigma}_y$ are evaluated. Three individual test results are averaged in each case and the standard deviation is given. In addition, the experiments are measured with a microDAC video extensometer and the in-plane von Mises strain ε_v is evaluated with VEDDAC 7 software (Chemnitzer Werkstoffmechanik GmbH, Germany).

2.2. Reconstruction of the as-built morphology of TPMS lattices

Additively manufactured TPMS lattices have external imperfections in terms of surface roughness and excess material, cf. Section 1. Previously, we developed a modeling procedure [50] in which the imperfect morphology of a lattice is artificially reconstructed rather than taken one-to-one from µ-CT scans. This procedure is adopted for the present study, so that only the essentials are outlined here. For distinction, the ideal CAD lattice is called as-designed model, the lattice derived directly from µ-CT data is called as-built model, and the artificially modeled lattice is called reconstructed model.

Modeling begins with mesh preparation using nTopology software (USA), which converts the raw surface mesh from the µ-CT scan into a smooth triangular surface mesh. This includes conversion to a voxel grid, smoothing and reconversion to a surface mesh, cf. **Fig. 3**. The impact associated with smoothing is discussed in Section 3.2. Note that the morphology of the as-built model is the reference for the reconstructed model.

Based on the as-designed model, the material is redistributed in a three-step modeling procedure, cf. **Fig. 4**. The modeling is done using MATLAB software and the z-direction corresponds to the BD. Firstly, the excess material is modeled on the overhanging surfaces. For a slope-dependent amount of excess material, the Zenith angle θ between the slope of the lattice surface and the z-axis is determined. Then, the z-coordinate of all surface nodes is shifted by the sigmoid function

$$g_1(\theta) = C_3 + \frac{C_4 - C_3}{1 + \exp\left(C_1(C_2 - \theta)\right)}, \tag{1}$$

where C_1 to C_4 control the course of the function.

In the second step, the surface roughness is generated by repeatedly shifting the surface nodes slightly with random size and direction. Specifically, an iteration loop is executed defining a random point within the design domain of the lattice and a random direction. Based on these quantities, the surface is shifted depending on the position. During one iteration, the direction of the shift remains constant for the entire surface. In contrast, the magnitude depends locally on the distance d to the random point according to

$$g_2(d) = C_5 \exp\left(-C_6\, d\right). \tag{2}$$

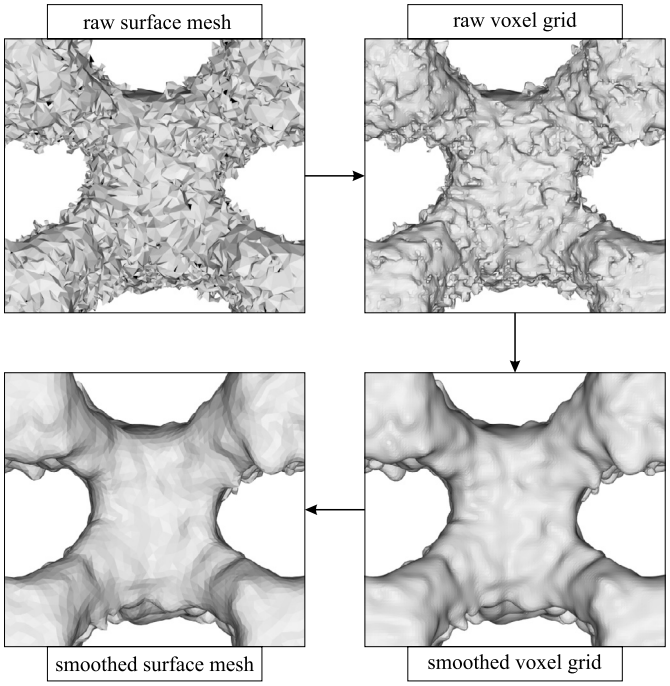

Fig. 3. Preparation of µ-CT data to create a smoothed surface mesh.

Again, C_5 and C_6 are modeling constants to be specified. The surface shifting is looped 2000 iterations per unit cell. To match the volume fraction φ of the reconstructed model to that of the as-built model after material redistribution, the level set constant r is readjusted in the third step.

The further modeling constants C_1 to C_6 are calibrated to minimize the relative Boolean difference volume Δ_{BOOL} between the as-built and the reconstructed model. Δ_{BOOL} is calculated by first subtracting the bounding volume of the reconstructed model from that of the as-built model, and then by dividing the remaining volume by the design space volume. This measurement is done with nTopology software. Unlike the volume fraction φ, which is the same in all three models, the relative Boolean difference volume Δ_{BOOL} indicates the morphological similarity and is therefore used. To facilitate the comparability of the different variants, a size-independent representation is used for the modeling parameters and the resulting shifts g_1 and g_2. For this purpose, all size-dependent values are related to the respective cell size of a model. Due to the semi-stochastic modeling procedure, no unique lattice design is obtained. Therefore, three lattices are considered for each parameter set and the standard deviation is given.

2.3. Finite element simulation

The FE modeling and simulation is performed with Pam-Crash 17.5 software (ESI Group, France) using the explicit solver. The triangular surface meshes of all models are converted into tetrahedral FE volume meshes with quadratic shape functions using nTopology software. h-refinement mesh studies are performed with 1% tolerance to determine the required number of elements.

The material model is primarily adopted from [50] and reflects the orthotropic elastoplastic behavior of LPBF processed Ti-42Nb. However, since the focus of this study is on compressive deformation behavior, no failure is modeled. The elastic material response is determined by nine constants: the elastic moduli E_{ii}, the shear moduli G_{ij} and the Poisson's ratios ν_{ij}, with $i, j = x, y, z$. The spatial directions x, y and z are the orthotropic axes of the material, with the z-direction corresponding to the BD.

The yield surface is described by the yield function of the Raghava-Hill plasticity model [53], which reads

Table 2
Parameters of the LPBF processed Ti-42Nb material model.

	parameter	value	unit
orthotropic elasticity	E_{xx}	60.0	GPa
	E_{yy}	60.0	GPa
	E_{zz}	64.0	GPa
	G_{xy}	21.5	GPa
	G_{yz}	26.0	GPa
	G_{zx}	26.0	GPa
	ν_{xy}	0.4	-
	ν_{yz}	0.4	-
	ν_{zx}	0.4	-
Raghava-Hill plasticity	F	1.2	-
	G	0.9	-
	H	1.0	-
	L	3.0	-
	M	3.0	-
	N	3.0	-
	α	1.2234	-
strain hardening	a	1000	MPa
	b	790	MPa
	n	0.8	-
	$\sigma_{\max}$	1400	MPa

$$f(\boldsymbol{\sigma}, \alpha, R) = \frac{3(\alpha-1)\,\sigma_{\mathrm{m}} + \sqrt{9\big((\alpha-1)\,\sigma_{\mathrm{m}}\big)^2 + 4\alpha\,\sigma_{\mathrm{H}}^2}}{2\alpha} - R. \tag{3}$$

Here, $\sigma_{\mathrm{m}} = \mathrm{tr}(\boldsymbol{\sigma})/3$ is the hydrostatic stress of the Cauchy stress tensor $\boldsymbol{\sigma}$ and R the current yield stress. The constant $\alpha = \sigma_{\mathrm{y}}^{\mathrm{c}}/\sigma_{\mathrm{y}}^{\mathrm{t}}$ measures the compression-tension ratio of the yield stress in compression $\sigma_{\mathrm{y}}^{\mathrm{c}}$ and tension $\sigma_{\mathrm{y}}^{\mathrm{t}}$. The effective Hill stress σ_{H} is defined by

$$\sigma_{\mathrm{H}} = F(\sigma_{yy}-\sigma_{zz})^2 + G(\sigma_{zz}-\sigma_{xx})^2 + H(\sigma_{xx}-\sigma_{yy})^2 + 2L\sigma_{yz}^2 + 2M\sigma_{zx}^2 + 2N\sigma_{xy}^2, \tag{4}$$

where F, G, H, L, M and N are constants describing the directionality of the yield function.

Strain hardening is characterized by a power law model according to

$$\sigma(\varepsilon_{\mathrm{p}}) = \min(a + b\,\varepsilon_{\mathrm{p}}^{n},\, \sigma_{\max}), \tag{5}$$

where a represents the initial yield stress, b the strain hardening coefficient, n the strain hardening exponent and $\sigma_{\max}$ the maximum allowable von Mises stress. ε_{p} denotes the effective plastic strain, which is calculated with the plastic deformation rate tensor $\boldsymbol{D}^{\mathrm{p}}$ at time t by

$$\varepsilon_{\mathrm{p}} = \int_0^t \sqrt{\frac{2}{3}\,D_{ij}^{\mathrm{p}}\,D_{ij}^{\mathrm{p}}}\,\mathrm{d}t. \tag{6}$$

The parameters of the material model are taken from [50] and listed in **Table 2**.

For the boundary conditions, two rigid plates are modeled at the top and bottom of a lattice, cf. **Fig. 5**(a). A surface-to-surface contact condition is used between the plate and lattice with a friction coefficient of 0.3. Self-penetration of the lattice is excluded by an additional contact condition. All degrees of freedom of the lower plate are restricted, whereas the upper plate is displaceable only in z-direction. The displacement applied to the upper plate is $\bar{u} = \bar{\varepsilon}\,l$ with the effective nominal strain $\bar{\varepsilon} = -0.3$.

During compression, the reaction force and displacement are captured. From this directly measured variables, nominal stress-strain curves are calculated analogously to the experiment in Section 2.1. Furthermore, the effective compressive stiffness $\bar{E}$ and the effective compressive yield strength $\bar{\sigma}_{\mathrm{y}}$ are considered for the numerical mechanical characterization. An example of data evaluation is given in **Fig. 5**(b). Finally, the contour plot of the von Mises equivalent strain ε_{v} is analyzed.

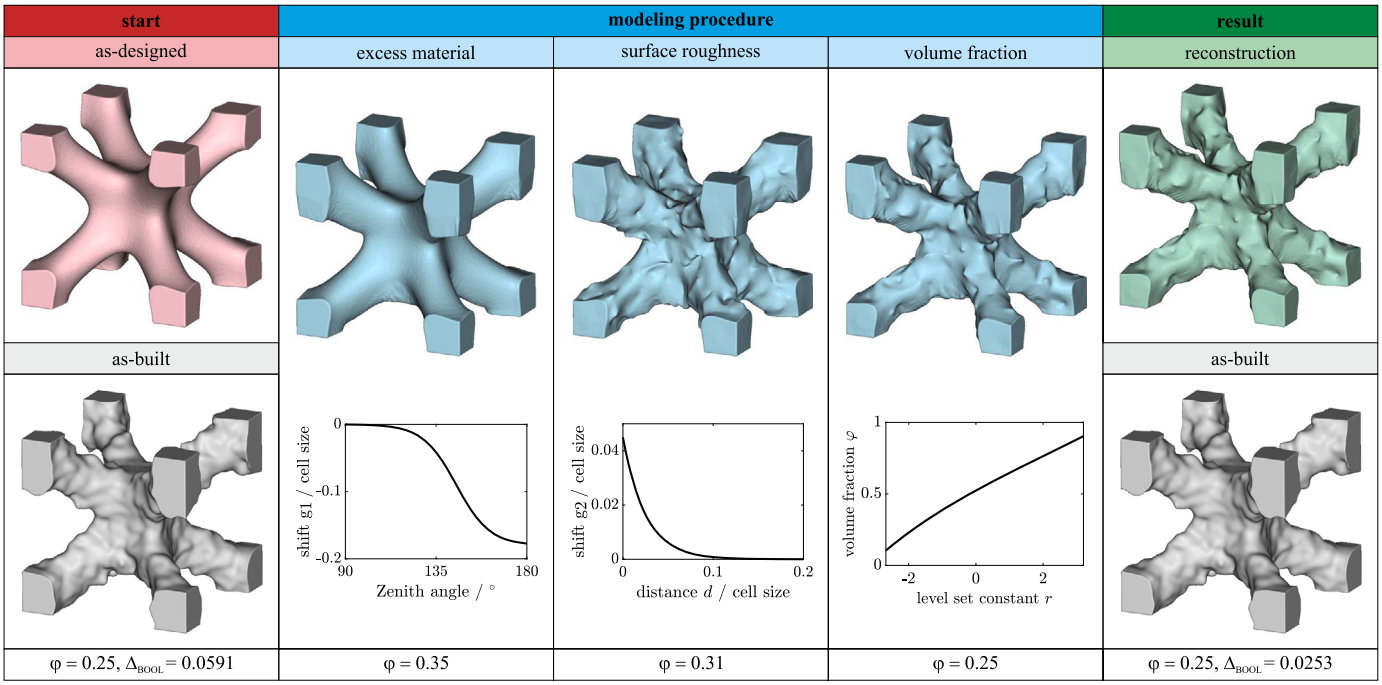

Fig. 4. Illustration of the TPMS lattice reconstruction described in Section 2.2.

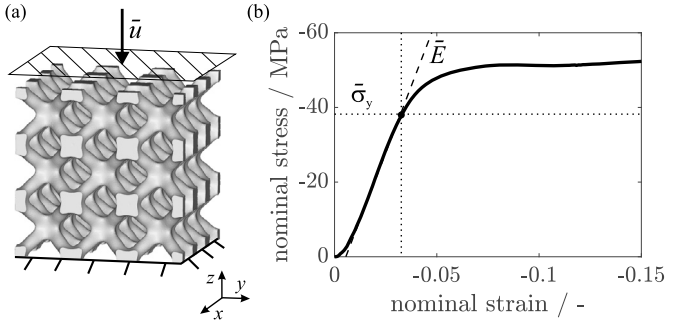

Fig. 5. Details of FE simulations: the boundary conditions are shown in (a) and the parameter evaluation in (b).

3. Results and discussion

In this section, the experimental and numerical results are discussed. In Section 3.1, the processed and modeled lattices are examined morphologically before in Section 3.2, the mechanical results are reviewed. Finally, extensions of the modeling procedure are investigated in Section 3.3.

3.1. Morphological results

The characteristic as-built morphology is illustrated by the digital microscopy images of modified Gyroid lattices with 2 mm and 4 mm cell size in **Fig. 6**. Although the TPMS morphology is principally well represented, three types of imperfections are observed. Firstly, partially molten powder particles adhere to the surface, resulting in increased roughness. The comparison between the top view and the side view in **Fig. 6**(a) and (b) shows only a slight difference in roughness for all lattices. Thus, without verification of the roughness parameters, an approximately homogeneous roughness distribution can be stated. For implants, an averaged surface roughness of up to 8.5 µm is positive for osseoconductivity [54]. However, from a mechanical standpoint, roughness is an issue that likely needs to be addressed through post-treatments, as the notch effect compromises the load-bearing capacity. This especially applies to components subjected to fatigue loads [32,55].

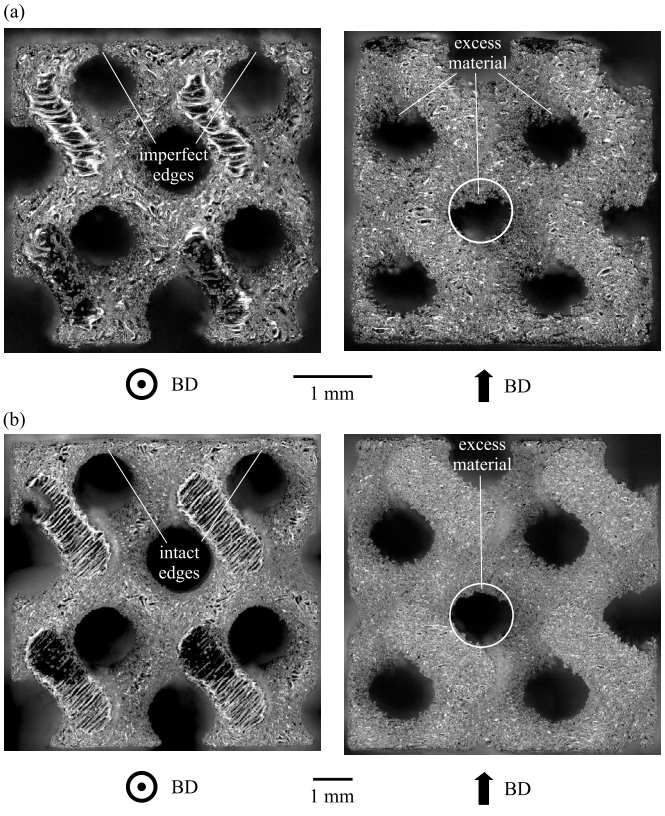

Fig. 6. Digital microscope images of (a) 2x2x2-G*-2 and (b) 2x2x2-G*-4 lattices, respectively in top and side view.

The second type of imperfection concerns the excess material on the overhanging surfaces, which is particularly evident in the side views of

Fig. 6. From the auxiliary circles drawn with the as-designed pore size, it is apparent that excess material depends on the cell size: here, the smaller the cell size is, the greater the relative amount of excess material. In terms of process physics, the phenomenon can be attributed to local overmelting because of impeded heat conduction into the powder. Consequently, the amount of excess material can be reduced by selectively reducing the energy input at the overhanging surfaces [17]. Finally, excess material entails a directionality of as-built morphology, whose mechanical implications are explored in Section **3.2**.

Thirdly, lattice edges prove to be zones of compromised structural integrity, where defects such as broken struts occur partially. On the one hand, this can be attributed to the lack of support from the adjacent struts already built. On the other hand, half-cut struts occur at the edge due to the design domain limitation, resulting in feature sizes below the permissible minimum. Similar to the relative amount of excess material, this defect type is subject to the cell size: the edges that are broken in the 2 mm cells in **Fig. 6**(a) are intact in the 4 mm cells in (b). In addition, the design modification of the Gyroid lattice proves to be effective, as filigree edges are largely avoided. In contrast, no qualitative effects on process fidelity are observed for the modified I-WP lattices.

The results of the target-actual comparison between as-designed and as-built state from the µ-CT scans are compiled in **Fig. 7**. Initially, general findings that apply to all models are discussed. Based on the spatial deviation plots in **Fig. 7**(a) and (b), a comparatively small deviation between ±100 µm is observed for the majority of the surfaces. In addition to this roughness-related deviation, up to 400 µm large deviation is detected due to excess material on overhanging surfaces. This becomes noticeable from 45° overhang and increases with increasing angle. The deviation measures are essentially in agreement with the literature. For example, Davoodi et al. [34] reported deviations of up to 340 µm for TPMS lattices made of Ti-6Al-4V, especially on overhanging surfaces. In the signed distribution plots in **Fig. 7**(c) and (d), roughness is reflected in a pronounced peak, whereas excess material leads to positive skewness. Similar results were found by Zou et al. [35] and Yang et al. [37] in their studies on LPBF processed TPMS lattices. Moreover, the excess material on overhanging surfaces is differently located in the lattices: while excess material in the I-WP lattice occurs mainly at the bottom of the nodes, in the Gyroid lattice it is also present below the struts.

Using the absolute deviation plot in **Fig. 7**(c), the size effect of imperfections can be further specified: accordingly, not only the relative deviation decreases with increasing cell size, but also the absolute deviation. This finding is explained by the improved heat dissipation due to the larger material volume, resulting in less partially melted particles [36,54]. The absolute deviation plot in **Fig. 7**(d) shows that the target-actual deviation for the modified lattices is smaller than for their respective reference variant. Thus, both presented design modifications prove to be quantitatively effective in terms of process fidelity. Specifically, this refers to the avoidance of filigree edges in the Gyroid lattice and to a uniform strut design in the I-WP lattice. Another important finding emerges from the comparison between both TPMS types investigated: regardless of cell size and design modification, the deviation is larger for the I-WP lattices than for the Gyroid lattices. This finding confirms conjectures from previous work [50] evaluating the LPBF-related criticality of TPMS lattices. In particular, it was found that for the I-WP lattice, about 15% of the surface has an overhang of at least 45°, compared to 11% for the Gyroid lattice. The resulting mechanical implications are discussed in the Sections **3.2** and **3.3**.

The production-related advantage of the Gyroid lattice over the I-WP lattice is also reflected in the deviation metrics in **Table 3**. In fact, the TPMS type appears to be the dominant factor for process fidelity, as up to 27.7% less mean deviations are obtained with the Gyroid variant. In contrast, doubling the cell size and design modifications result in up to 18.6% less mean deviation. Furthermore, it is found that the volume fraction of all models exceeds the target value of 0.25. Here, the lattices with 2 x 2 x 2 unit cells tend to have larger volume fractions than those with 3 x 3 x 3 cells. This can be attributed to the lower cell count, where edge defects have a greater effect [30]. In general, exceeding the target volume fraction is a commonly observed phenomenon in PBF processed components resulting from material adhesions [34,56,57]. However, subtractive post-treatments such as etching [31], pickling [58] or sandblasting [33] can generally be used to adjust the desired volume fraction. Finally, µ-CT measurements of microporosity show values less than 0.2% for all specimens, indicating adequate process control.

Now that the as-built morphology has been studied, the reconstruction is performed. The parameter space of the I-WP model is shown in **Fig. 8**(a). Starting from the standard design ⓪, morphological derivatives are modeled by applying the shifts g_1 and g_2 using Eqs. (**1**) and (**2**): if the shifts are applied separately, models with either excess material ① or surface roughness ② are obtained. Combining both shifts results in models with both excess material and roughness ③. By parameter selection, the proportions of both defect types can be adjusted until a given as-built morphology is reconstructed ④. As described in Section **2.2**, the volume fraction for the entire parameter space is equal to that of the µ-CT measurement. Furthermore, for better comparability of the reconstructed models, besides the level set constant r only the scaling parameters C_4 and C_5 are varied.

To find an optimal solution, the relative Boolean difference volume between as-built and reconstructed model Δ_{BOOL} is first computed for numerous discrete parameter tuples, cf. **Fig. 8**(b). Cubic surface interpolation with MATLAB then yields the continuous deviation map in **Fig. 8**(c), which contains information about the reconstruction quality for the entire parameter space. The crucial point here is that a convex optimization problem with a unique solution is obtained. The optimal parameter sets determined in this way are listed in **Table 4** for all models. Here, the amount of C_4 for the excess material exceeds that of C_5 for the roughness by a factor of three to four. This relation fits in principle to the experimental results. In addition, the experimentally observed cell size effect is reflected in a degressive proportionality between cell size and absolute shift amounts expressed in C_4 and C_5: when doubling the cell size, the relative shift amounts are less than halved. Note that the modeling parameters inherently depend on the material-process combination. Therefore, the identified parameters apply only to the specific manufacturing process studied here.

Fig. 9 contains the side views of all as-designed, as-built and reconstructed models, as well as their morphological metrics in terms of relative Boolean difference volume Δ_{BOOL} and mean absolute deviation MD. Overall, the effectiveness of the modeling procedure is demonstrated as the morphological similarity between the reconstructed and as-built models is significantly higher than that between the as-designed and as-built models: in particular, Δ_{BOOL} decreases approximately by half, and MD largely matches that of the µ-CT measurement for each model. This finding confirms the results for the single I-WP lattice studied in [50]. However, there is still a discrepancy between the as-built and the reconstructed models: on the one hand, this can be attributed to the fact that three reconstructions are used for each variant. This avoids overfitting the modeling parameters, but the reconstruction is not optimal for a single specimen. On the other hand, the reconstruction procedure used does not reflect the particular defect susceptibility of peripheral lattice zones. Consequently, although the modeled degree of imperfections is similar on average to the as-built lattice, it is too small at the lattice periphery and too large at the center. An adapted, position-dependent reconstruction procedure allows to address this issue in the future.

Comparing the different models, two important observations emerge: firstly, the two morphological metrics Δ_{BOOL} and MD tend to correlate. Thus, the regularities found for the mean absolute deviation in **Table 3** also apply to the relative Boolean difference volume. This is particularly evident from the influence of design modification shown in the bottom half in **Fig. 9**. However, when considering different cell sizes (upper half), this tendency is overlaid by a second effect: Δ_{BOOL} de-

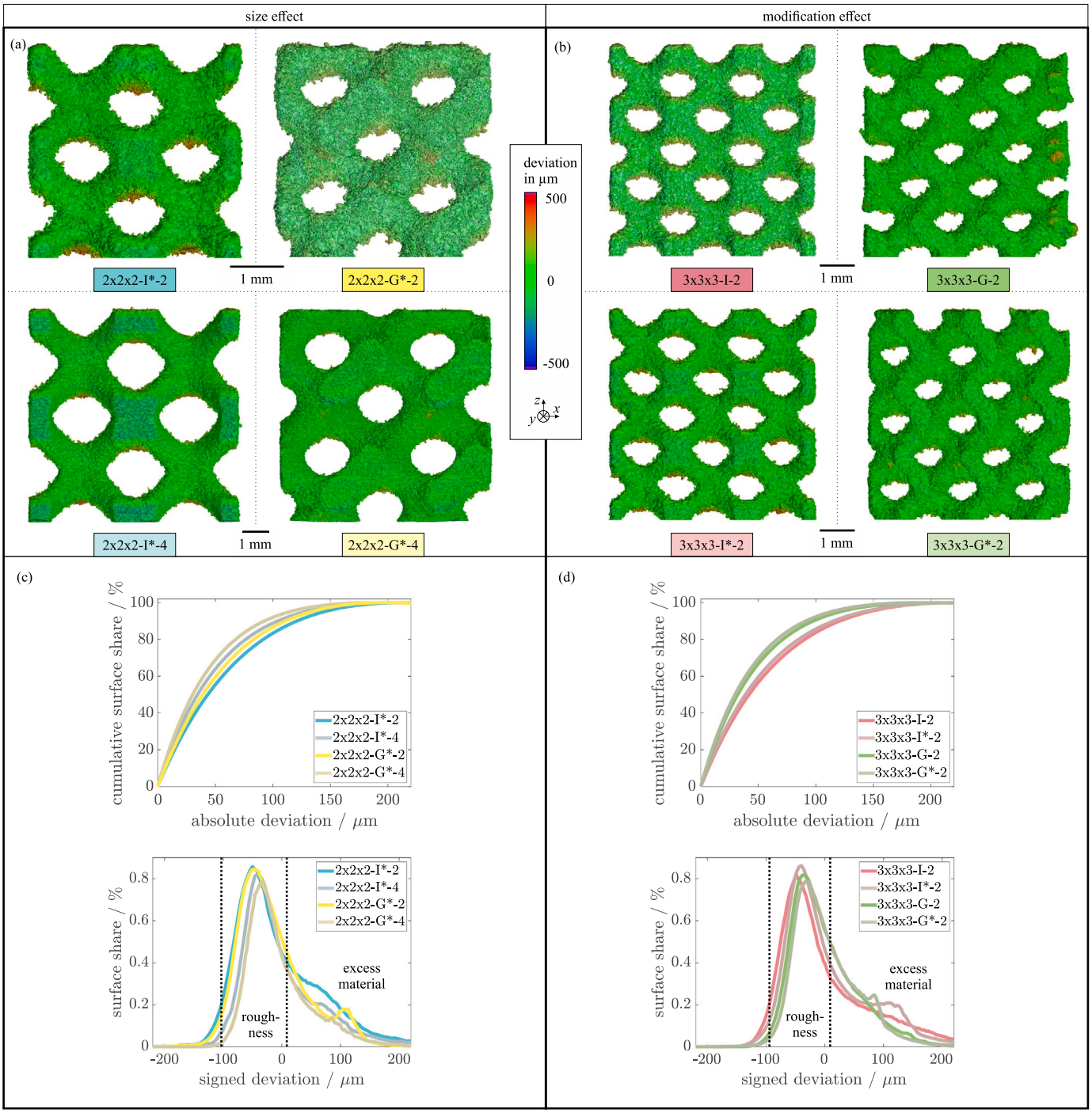

Fig. 7. Morphological data from µ-CT scans: in (a) and (b), the three-dimensional deviation plots are shown, and in (c) and (d), the distributions of the deviation over the surfaces. The quantities refer to the deviation between the as-designed and the as-built model. Left is the comparison for the size effect and right for the modification effect. The division drawn in the signed distribution plots in (c) and (d) serves for qualitative differentiation according to roughness and excess material. The model designations refer to **Table 1**.

creases by up to 93% when the cell size is doubled, while MD only decreases up to 16.3%. This difference is due to the geometrical size effect, which is only reflected in the relative Boolean difference volume but not in the mean absolute deviation. Thus, the relative Boolean difference volume Δ_{BOOL} proves to be a more pertinent descriptor for the effective morphological similarity of two structures than the mean absolute deviation MD. The mechanical implications are investigated in the following section.

3.2. Mechanical results

In this section, the uniaxial quasi-static compressive behavior of TPMS lattices is investigated. Starting with the experimental results, the nominal stress-strain curves are presented in **Fig. 10**(a) and (b). In general, a pronounced plastic domain with horizontal curve progression is observed for all eight variants. In particular, the lattices pass 30% nominal strain without abrupt failure, which contributes to a safe implant

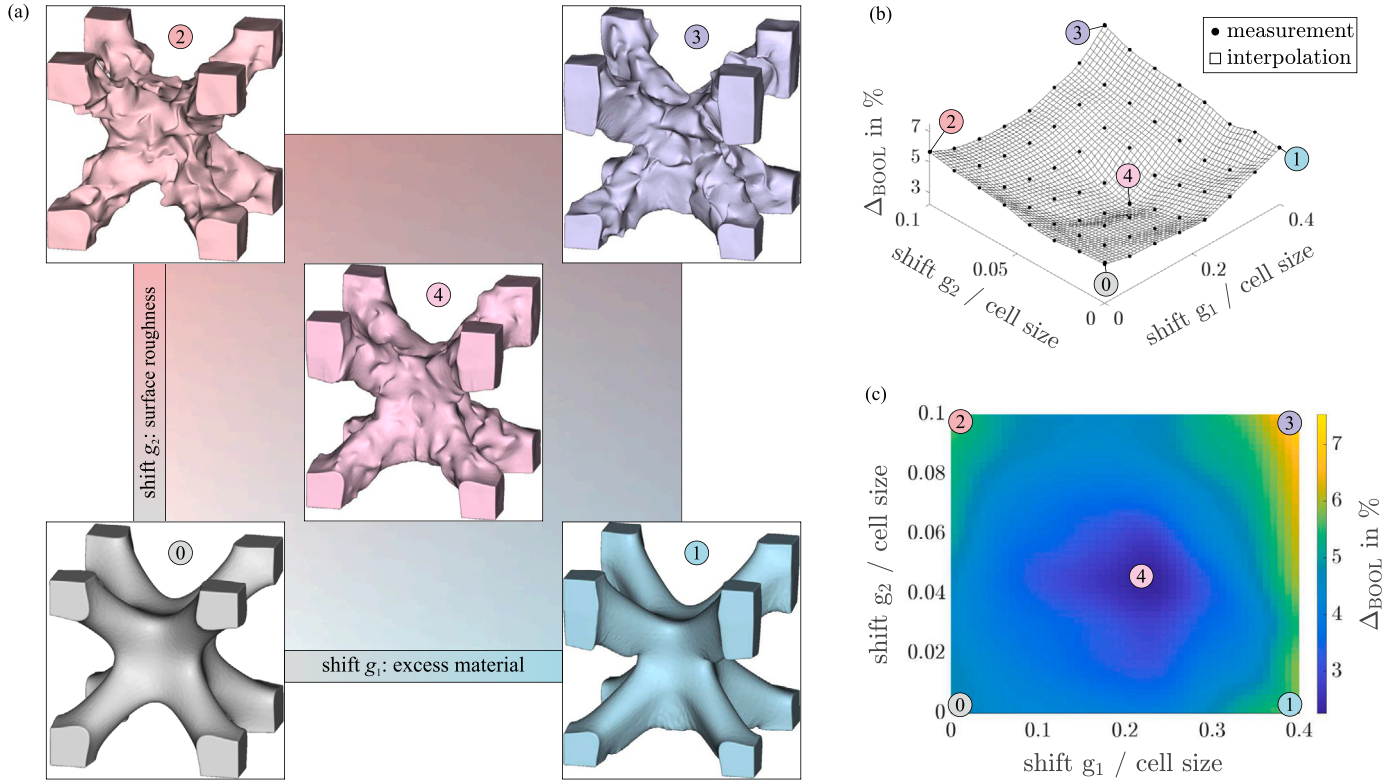

Fig. 8. Parameter calibration of the reconstruction exemplified by an I-WP lattice: in (a), the topology of the parameter space is shown qualitatively, and in (b) and (c) the parameter space is correlated with the relative Boolean difference volume Δ_{BOOL} with respect to the as-built model.

Table 3
Morphological metrics from µ-CT scans: φ denotes volume fraction, where the target value is 0.25, MD is the mean absolute deviation, $Q10$, $Q50$ and $Q90$ are the 10%, 50% and 90% quantiles of cumulative absolute deviation, and $\Delta_{rel.}$ is the relative deviation.

TPMS lattice	φ	MD / µm	$\Delta_{rel.}$(MD)	$Q10$ / µm	$\Delta_{rel.}(Q10)$	$Q50$ / µm	$\Delta_{rel.}(Q50)$	$Q90$ / µm	$\Delta_{rel.}(Q90)$
2x2x2-I*-2	0.2729	59.783	0.1473	7.0021	0.2885	43.528	0.2568	121.04	0.1615
2x2x2-I*-4	0.2631	52.108		5.4342		34.635		104.21	
2x2x2-G*-2	0.2654	51.139	0.1859	6.3543	0.3335	39.124	0.2828	110.52	0.1915
2x2x2-G*-4	0.2627	43.122		4.765		30.498		92.756	
3x3x3-I-2	0.2626	66.025	0.1542	6.6347	0.0658	41.067	0.072	120.59	0.0447
3x3x3-I*-2	0.2625	57.201		6.2251		38.308		115.43	
3x3x3-G-2	0.2611	51.971	0.1606	5.5899	0.1986	36.924	0.2593	99.299	0.089
3x3x3-G*-2	0.259	44.778		4.6638		29.321		91.184	

Table 4
Modeling parameters for the reconstructed models of imperfect TPMS lattices according to Section 2.2.

TPMS lattice	C_1	C_2	C_3 / cell size	C_4 / cell size	C_5 / cell size	C_6	r
2x2x2-I*-2	0.1	150	0	−0.1632	0.0438	3	−2.2434
2x2x2-I*-4	0.1	150	0	−0.0773	0.0214	3	−2.1153
2x2x2-G*-2	0.1	150	0	−0.146	0.0485	3	−0.8255
2x2x2-G*-4	0.1	150	0	−0.0687	0.0236	3	−0.7958
3x3x3-I-2	0.1	150	0	−0.1813	0.0452	3	−2.2825
3x3x3-I*-2	0.1	150	0	−0.1293	0.0405	3	−2.1872
3x3x3-G-2	0.1	150	0	−0.1604	0.0399	3	−0.8135
3x3x3-G*-2	0.1	150	0	−0.1297	0.0468	3	−0.8042

application in BTE. This excellent deformability of TPMS based lattices made of Ti-42Nb confirms previous results [50].

As with the morphology in Section 3.1, cell size and design modifications are reflected in the mechanical results: both the 4 mm unit cell size and the modified design are associated with improved mechanical performance in terms of stiffness and strength compared to the reference variants, cf. **Fig. 10**(a) and (b). This is due to the better process fidelity, *i.e.*, the lower degree of imperfections. Noteworthy is the direct correlation between the relative Boolean difference volume Δ_{BOOL} from **Fig. 9** and the mechanical properties. In all four comparisons (two each for the size effect and modification effect), the stiffness and strength of the model with lower Δ_{BOOL} are greater than the respective counterpart. Moreover, stiffness and strength are found to decrease for parallel test direction (∥) compared to perpendicular direction (⊥). This directionality of mechanical properties can be attributed to the excess material on overhanging surfaces causing morphological anisotropy. However,

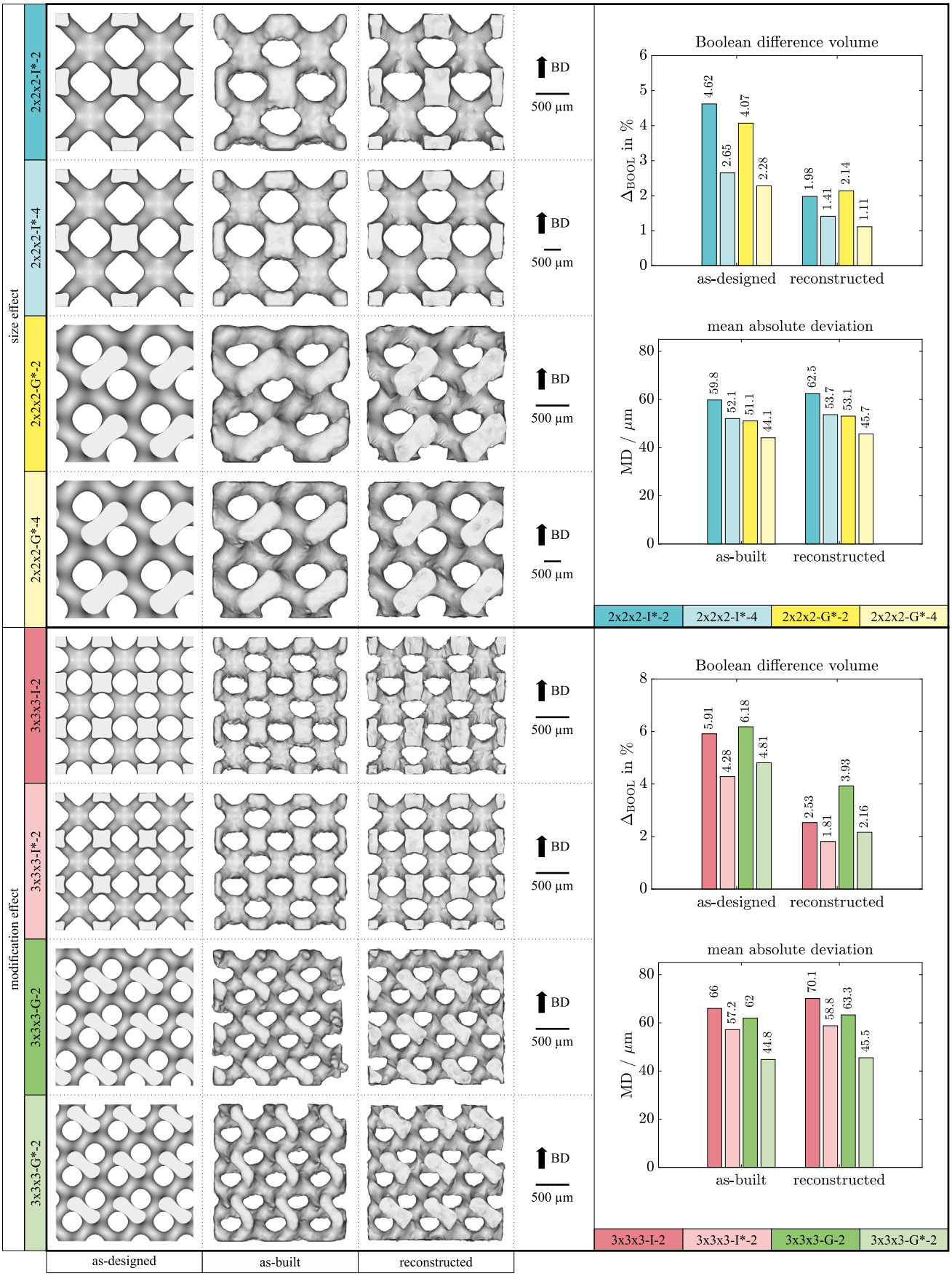

Fig. 9. Morphological results: Δ_{BOOL} is the relative Boolean difference volume to the as-built model and MD is the mean absolute deviation to the as-designed model. The model designations refer to **Table 1**.

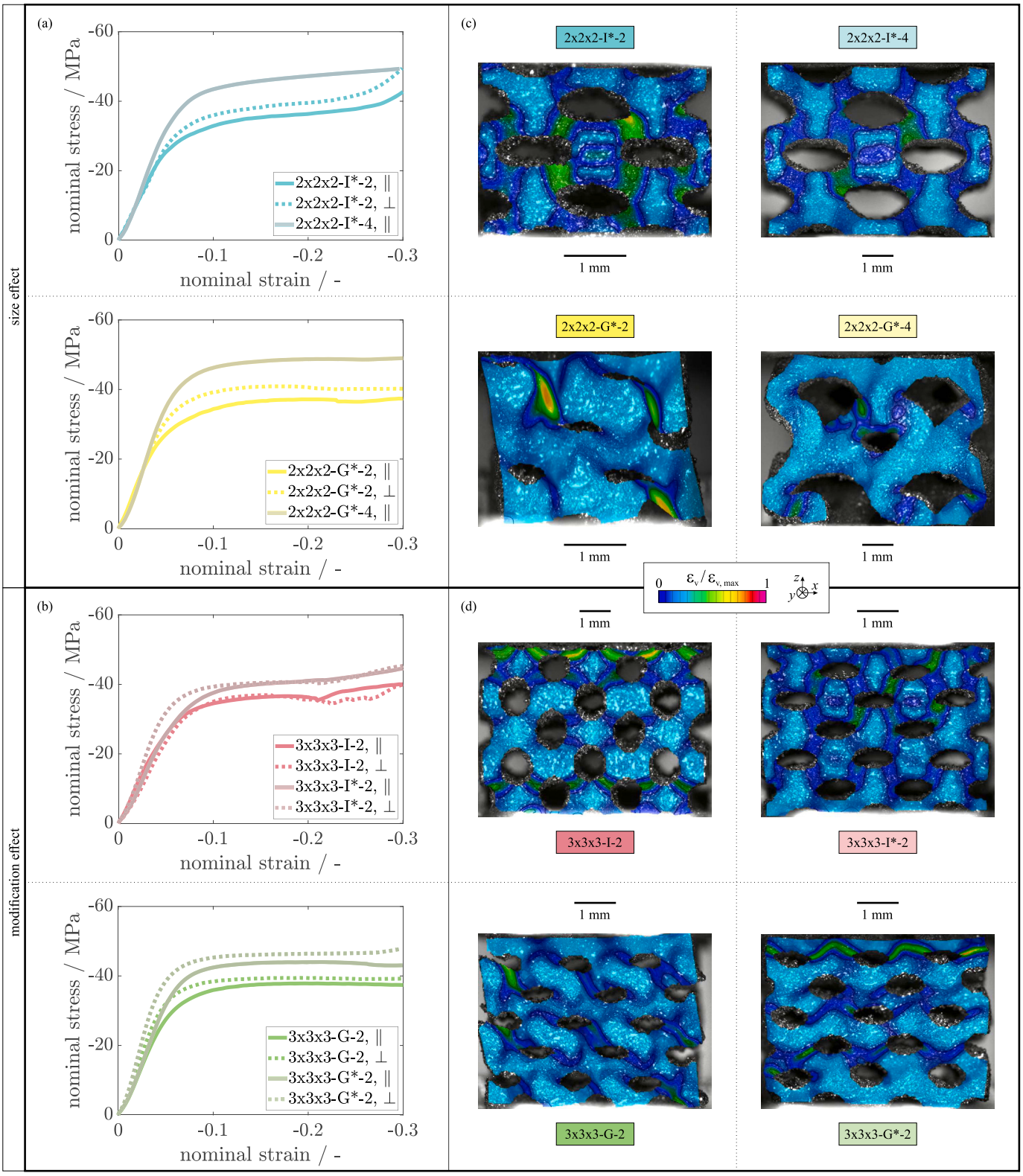

Fig. 10. Experimental results of compression tests: in (a) and (b), the nominal stress-strain curves averaged from three specimens each are shown for parallel (||) and perpendicular (⊥) test directions, and in (c) and (d), the in-plane von Mises strain distributions for $\bar{\varepsilon} = -0.15$ applied nominal strain determined with DIC. The upper half shows the effect of cell size and the lower half that of design modification. The model designations refer to **Table 1**.

the influence of test direction is less than that of cell size and design modification.

To further investigate the compressive behavior, the in-plane von Mises strain maps in **Fig. 10**(c) and (d) are considered. These refer to the parallel test direction and $\bar{\varepsilon} = -0.15$ applied nominal strain. Compared to the 4 mm cell size, the 2 mm variants exhibit a more heterogeneous strain distribution, cf. **Fig. 10**(c). This is due to the greater influence of imperfections at smaller cell sizes. In fact, imperfections under loading

Table 5
Experimental results from uniaxial compression tests determined from the average of three specimens for parallel and perpendicular test directions, respectively: $\Delta_{rel.}$ denotes the relative deviation for either compressive effective stiffness $\bar{E}$ or yield strength $\bar{\sigma}_y$.

TPMS lattice	parallel				perpendicular			
	$\bar{E}$ / MPa	$\Delta_{rel.}(\bar{E})$	$\bar{\sigma}_y$ / MPa	$\Delta_{rel.}(\bar{\sigma}_y)$	$\bar{E}$ / MPa	$\Delta_{rel.}(\bar{E})$	$\bar{\sigma}_y$ / MPa	$\Delta_{rel.}(\bar{\sigma}_y)$
2x2x2-I*-2	571.1 ± 44.3	0.254	23.61 ± 1.27	0.449	585.2 ± 37.4	-	25.81 ± 1.13	-
2x2x2-I*-4	716.4 ± 61.0		34.22 ± 2.02		-		-	
2x2x2-G*-2	709.3 ± 49.8	0.1	26.51 ± 1.22	0.445	733.2 ± 64.7	-	29.82 ± 1.56	-
2x2x2-G*-4	780.4 ± 67.3		38.31 ± 1.73		-		-	
3x3x3-I-2	587.3 ± 39.1	0.043	26.44 ± 1.68	0.222	512.2 ± 56.2	0.43	29.38 ± 2.12	0.109
3x3x3-I*-2	612.4 ± 35.7		32.30 ± 1.45		732.4 ± 80.7		32.59 ± 1.78	
3x3x3-G-2	653.6 ± 46.7	0.047	28.04 ± 1.62	0.276	803.9 ± 87.5	0.163	30.48 ± 1.77	0.244
3x3x3-G*-2	684.3 ± 56.0		35.79 ± 1.91		934.7 ± 77.3		37.91 ± 2.23	

Table 6
Numerical results of uniaxial compression tests in parallel with BD using the as-designed, as-built or reconstructed lattice morphology: $\Delta_{rel.}$ denotes the relative deviation from experimental results for compressive effective stiffness $\bar{E}$ or yield strength $\bar{\sigma}_y$.

TPMS lattice	as-designed		as-built		reconstructed	
	$\Delta_{rel.}(\bar{E})$	$\Delta_{rel.}(\bar{\sigma}_y)$	$\Delta_{rel.}(\bar{E})$	$\Delta_{rel.}(\bar{\sigma}_y)$	$\Delta_{rel.}(\bar{E})$	$\Delta_{rel.}(\bar{\sigma}_y)$
2x2x2-I*-2	3.4123	0.6624	0.2247	0.1601	0.0534 ± 0.0262	0.1177 ± 0.0051
2x2x2-I*-4	2.5196	0.1952	0.3772	0.0488	0.1736 ± 0.0221	0.0129 ± 0.0062
2x2x2-G*-2	2.0792	0.6181	0.1143	0.0411	−0.0298 ± 0.0244	0.0323 ± 0.0057
2x2x2-G*-4	1.7987	0.0756	0.2837	−0.0321	0.2631 ± 0.0231	−0.0328 ± 0.0064
3x3x3-I-2	2.7088	0.4102	−0.0854	0.0377	−0.0322 ± 0.0247	0.0181 ± 0.0046
3x3x3-I*-2	2.6418	0.2021	−0.0915	−0.0602	−0.0281 ± 0.0221	−0.0042 ± 0.0045
3x3x3-G-2	2.5941	0.3293	0.0744	−0.0211	−0.1067 ± 0.0277	−0.0486 ± 0.0061
3x3x3-G*-2	2.5984	0.1504	0.1245	−0.0646	−0.0771 ± 0.0281	−0.08 ± 0.0056

cause local stress or strain concentrations that act as mechanical weak points. Focusing on the I-WP lattices in **Fig. 10**(d), the modified design appears to exhibit a more uniform strain distribution than the standard design. In particular, the thickened struts seem to be less critical to failure. The modification of the Gyroid lattice is also accompanied by a different failure mode: due to the modified edges, the lattices are primarily deformed by compression rather than by shear-like sliding. This leads to a layer-by-layer collapse of the modified lattices 90° to the loading direction [1,49].

In **Table 5**, the compressive effective stiffness $\bar{E}$ and yield strength $\bar{\sigma}_y$ are listed for all variants. Here, various influencing factors on the mechanical values are apparent. Besides the already discussed influences of cell size, design modification and test direction, the TPMS type turns out to be an important factor: in fact, the stiffness and strength of all Gyroid lattices are greater than the corresponding I-WP lattices. Depending on the variant, this increase is up to 24.2% in stiffness and 16.3% in strength. This finding is consistent with those of Cai et al. [59]. However, Torres-Sanches et al. [2] reported opposite results, which is probably due to the influence of imperfections. Another tendency is related to the cell number: the greater the cell number is, the greater the stiffness and strength. Although there are exceptions, especially in stiffness, the increase is up to 25.2%. On the one hand, this can be attributed to the greater influence of edge defects found in Section **3.1**. On the other hand, a lower cell number increases the proportion of less constrained edge cells, which deform more compliantly [30]. However, compared to the other influencing factors, cell size proved to be the most decisive factor with up to 25.4% stiffness gain and 44.9% strength gain. Therefore, the mechanical implications of cell size are further explored in Section **3.3**. In terms of absolute values, especially the modified Gyroid variants demonstrate excellent suitability for implant applications: with stiffnesses below 1 GPa and yield strengths above 35 MPa, the risk of a stress-shielding effect is minimized while ensuring structural integrity [10,11,60]. In order to optimize the mechanical properties of the scaffolds, shape optimization could also be considered in the future [52].

Finally, the results of numerical compression tests for parallel test direction are examined. Comparison of the nominal stress-strain curves of the as-designed, as-built and reconstructed models with those of the experiment in **Fig. 11** highlights two main aspects: firstly, regardless of the variant, the as-designed model overestimates the experimentally measured compression behavior. In contrast, secondly, both the as-built and the reconstructed model accurately represent the actual behavior. Both observations are consistent with pertinent literature [47,61]. It is important to remark that the volume fraction of all models considered is respectively equal to that of the experiment. Thus, a direct correlation between the target-actual deviation of the as-built morphology and the mechanical degradation is observed. More precisely, the imperfections included in the reconstruction, namely surface roughness and excess material, emerge as formative factors for quasi-static mechanical performance. In contrast, microporosity and material heterogeneity appear to be less important, as the as-built and reconstructed models accurately represent the experiment even without their consideration.

Causes for this finding arise from the von Mises strain distribution of the reconstructed models at a nominal strain of $\bar{\varepsilon} = -0.15$. On the one hand, excess material on overhanging surfaces is found to have subordinate load-bearing function. These ineffective material reservoirs are particularly evident in the I-WP lattices, where the excess material is located at the node bottoms, cf. Section **3.1**. Since the total material content is constant, other structural features such as the struts are thinned, *i.e.*, mechanically weakened. On the other hand, similar to the DIC plots in **Fig. 10**, a heterogeneous strain distribution with local peaks is shown. This is particularly pronounced in Gyroid lattices and can be attributed to the roughness-induced morphological irregularity. The mechanical degradation distribution with respect to excess material and roughness is further investigated in Section **3.3**.

The relative deviations from the experimentally measured compressive effective stiffness $\bar{E}$ and yield strength $\bar{\sigma}_y$ are listed in **Table 6** for all models. As expected, the as-designed models are subject to the largest deviations. This overestimation of stiffness is up to 340% and that of yield strength up to 66%. In contrast, the as-built and reconstructed models are associated with substantially lower deviations. In comparison, the reconstructed models tend to be the most precise, with a maximum deviation of 26% for stiffness and 12% for strength.

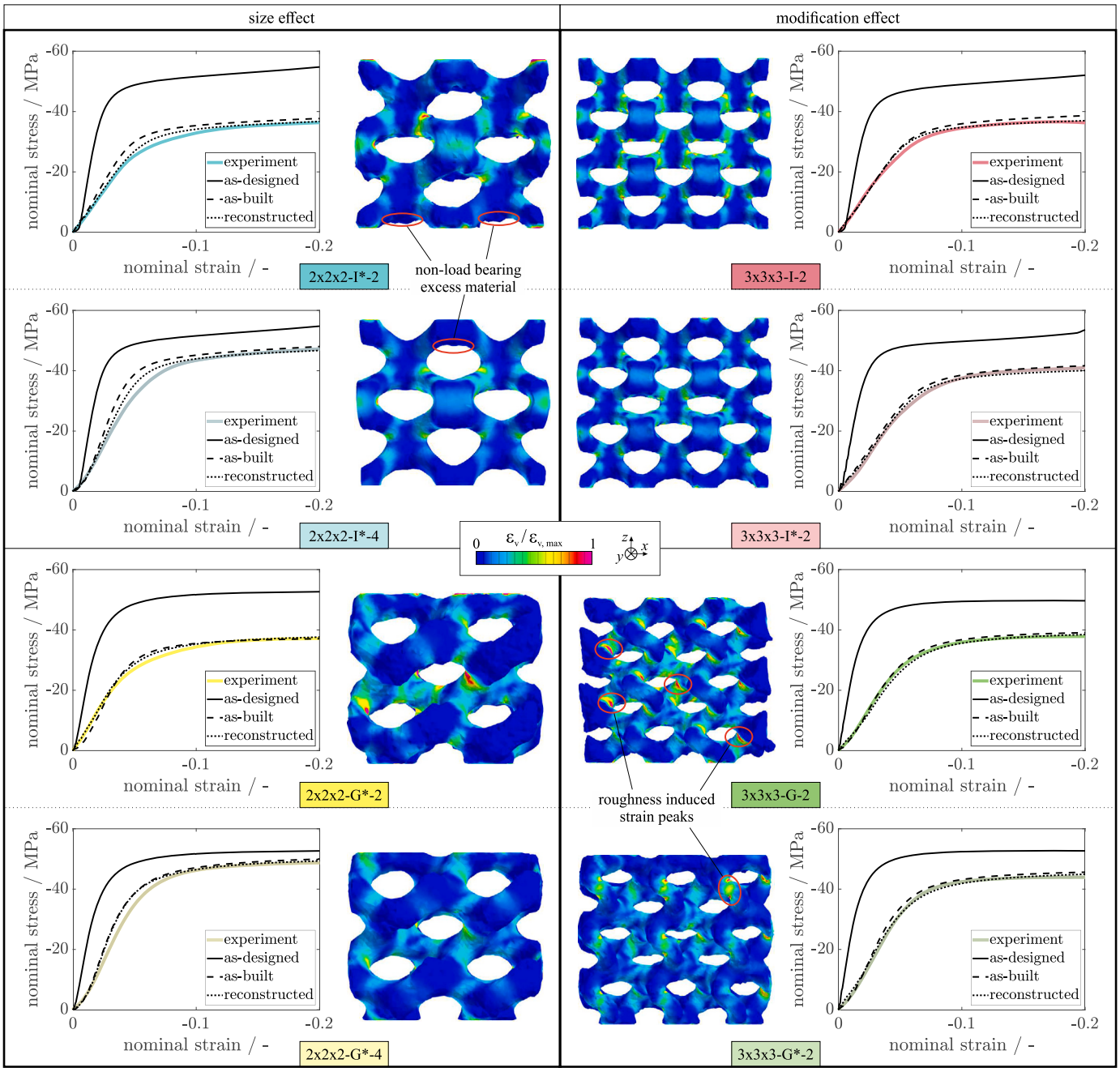

Fig. 11. Numerical results of uniaxial compression tests in parallel with BD: the nominal stress-strain curves obtained from FE simulations are compared with the experimental results from **Fig. 10**, and the von Mises strain plots refer to the reconstructed lattices at $\bar{\varepsilon} = -0.15$. Note that in each of the eight cases, the volume fraction of the numerical models is respectively equal to that of the experiment given in **Table 3**, whereas the material model specified in Section **2.3** is maintained in all simulations. The model designations refer to **Table 1**.

Here, it is important to note that the deviation between as-built and reconstructed morphology (cf. Section **3.1**) does not significantly affect the nominal mechanical properties of a lattice. In particular, the globally averaged degree of imperfection allows to accurately represent the quasi-static compressive behavior. Literature review indicates the effectiveness of the presented approach: Lozanovski et al. [47] found 23% and 31% numerical deviation for stiffness and strength for face-centered cubic lattices, and Radlof et al. [61] reported 153% and 28% for uniform cubic lattices, respectively. Since three specimens are considered for each of the experiments and reconstructed models, overfitting for a single specimen is ruled out. Furthermore, principally similar results are observed for the perpendicular test direction. Thus, the results are statistically significant, reproducible and generally valid.

Overall, the reconstruction procedure proves to be a valuable tool for non-destructive structure-property studies. In addition to the high morphological similarity noted in Section **3.1**, the FE analyses on the reconstructed models in this section attest to high simulation accuracy. This finding confirms that of previous work on a single lattice [50]. However, by considering different TPMS types, cell numbers, cell sizes and loading directions, the reproducibility and generalizability of the modeling approach is now also demonstrated. In the context of BTE scaffolds, high numerical accuracy can help to reduce the necessary testing effort without compromising optimal and safe application. Finally, the convincing findings suggest to use the procedure for more elaborated structure-property investigations. Therefore, two further issues are numerically explored in the next section.

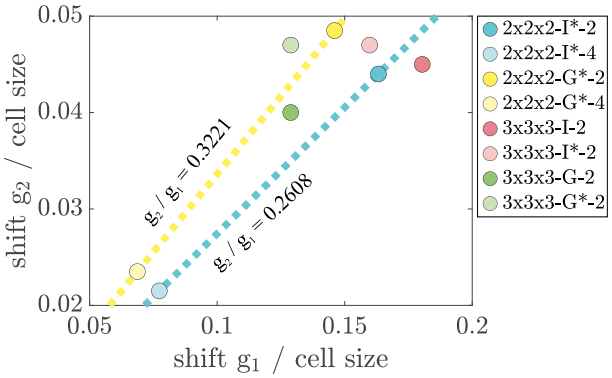

Fig. 12. Modeling parameters of excess material C_4 and surface roughness C_5 from **Table 4** in g_1-g_2-diagram for all reconstructed models: the plotted lines illustrate the influence of cell size on the parameters. The model designations refer to **Table 1**.

3.3. Numerical extension

So far, the reconstruction procedure has been used to fit the numerical TPMS morphology to that measured by µ-CT scan to simulate the compression behavior. In this section, the procedure is used for advanced numerical investigations: firstly, the size effect of mechanical degradation observed in Section 3.2 is quantified by a generalized regression model. This is to predict the actual mechanical behavior of I-WP and Gyroid lattices for arbitrary cell sizes. Secondly, the respective share of roughness and excess material in the total mechanical degradation is investigated. Such a degradation distribution provides information about which type of process-related imperfection is critical for the mechanical properties. Furthermore, it reveals the performance gain to be expected from morphology-modifying post-treatments such as sandblasting [32,33] and chemical polishing [31].

Starting with the size effect, the modeling parameters C_4 and C_5 from **Table 4** are first plotted in a g_1-g_2-diagram, cf. **Fig. 12**. Assuming a linear relationship, the size effect is expressed in terms of the slope between the data points of the 2 mm and 4 mm large cells. For both TPMS types, a positive slope is found as a result of the cell size dependence of the target-actual deviation: the smaller the cell size is, the larger the deviation is both in absolute and relative terms, cf. Section 3.1. Comparing both TPMS types, the excess material, *i.e.*, shift g_1, in the I-WP lattices exceeds that of the Gyroid lattices for any cell size. In contrast, roughness, *i.e.*, shift g_2, is more pronounced in the Gyroid lattices. This difference is an expression of the difference in additive manufacturability or the extent of overhang, cf. Section 3.1.

To further investigate the size-dependent mechanical degradation of I-WP and Gyroid lattices, nine reconstructions of different cell sizes between 1 - 5 mm are prepared, respectively. The shift amounts g_1 and g_2 are derived from the curves shown in **Fig. 12**. In fact, experimentally validated results for 2 mm and 4 mm large cells are thus inter- and extrapolated. Subsequently, numerical compression tests are performed in parallel and perpendicular to the BD. In **Fig. 13**(a) and (b), the stress distributions for lattices with 1 mm and 5 mm large cells are shown for both test directions. In addition, an overview of the differently sized reconstructions is given. Using cubic surface interpolation with MATLAB, the resulting discrete nominal stress-strain curves are transferred into continuous stress-strain surfaces that depend on the cell size. For the parallel test direction, these diagrams are shown in **Fig. 13**(c) and (d). Finally, the size-dependent compressive effective stiffness and yield strength are determined from the stress-strain surfaces. These are illustrated in **Fig. 13**(e).

As expected, stiffness and strength increase with increasing cell size. This applies to I-WP and Gyroid lattices in both parallel and perpendicular test directions. The reason is the size dependency of the target-actual deviation: besides the geometrically caused increase of the relative deviation with decreasing cell sizes, the absolute deviation also increases due to process physics, cf. Section 3.1. Together, this leads to an above-average increase in relative deviation as cell sizes decrease. This numerical finding is consistent with relevant literature reports, cf. [62]. Remarkably, this degressive size effect is also reflected in the mechanical properties: firstly, in **Fig. 13**(a) and (b), the lattices with 1 mm cell size exhibit higher peak stresses and a more heterogeneous stress distribution compared to those with 5 mm. This observation is consistent with the previous results, cf. **Fig. 10**(c) and **Fig. 11**. Secondly, stiffness and strength increase sharply at small cell sizes (<3 mm) until they approach a limit at larger cell sizes (>5 mm), cf. **Fig. 13**(e).

Another peculiarity emerges regarding the convergence behavior of stiffness and strength: the curves of parallel and perpendicular test directions tend to converge with increasing cell sizes. This is particularly obvious for the I-WP lattice. Two effects are responsible for this phenomenon: firstly, as stated in Section 3.2, the anisotropy of the target-actual deviation is immediately reflected in the mechanical properties. In particular, stiffness and strength in parallel to the BD were found to be reduced compared to those perpendicular to the BD. Since the relative deviation and mechanical degradation decrease with increasing cell size, both curves approach the result of the as-designed morphology. The still existing difference in the Gyroid lattice is explained by the second effect, which is the geometric anisotropy: unlike the I-WP lattice, the Gyroid lattice is not symmetrical with respect to the three spatial directions. Consequently, as long as a finite number of cells is considered, stiffness and strength differ in the two test directions.

Finally, Gyroid lattices exhibit greater stiffnesses and strengths than their I-WP counterparts for all cell sizes. Specifically, the stiffness of the Gyroid ranges between approximately 630 - 795 MPa and that of the I-WP ranges between 485 - 720 MPa. Simultaneously, the strength ranges from 20 - 41 MPa and 16.5 - 36 MPa for Gyroid and I-WP, respectively. Remarkably, the smaller the cell size is, the greater the quantitative difference between the two lattice types. This is due to better additive manufacturability of the Gyroid lattice and confirms previous results [50,63]. Overall, the selective experimental results from Section 3.2 fit well with the numerical results. Future experimental studies with additional cell sizes allow more rigorous verification of the predictions.

Now that the mechanical size effect has been investigated numerically, the question arises as to how the degradation is composed. To determine the associated degradation distribution, the experimentally validated parameter path for cell size is abandoned and an extended parameter space is considered instead. In particular, firstly, 7 x 7 models with different g_1-g_2-tuples are prepared for the I-WP and Gyroid type, respectively. Here, the tuples are selected systematically and span the parameter space 0 - 0.4 shift g_1 / cell size and 0 - 0.1 shift g_2 / cell size. Subsequently, numerical compression tests are performed in parallel with the BD. For the resulting stiffnesses and strengths, the relative deviations $\Delta_{rel.}$ to the values obtained from the as-designed models are calculated. To increase statistical significance, the results of three separate models are averaged for each parameter set. Finally, cubic surface interpolation is applied to the discrete data points using MATLAB. The resulting continuous stiffness and strength degradation diagrams are shown in **Fig. 14**(a) and (b). Here, the straight lines of the size effect defined in **Fig. 12** are drawn as well as the parameter sets for 1 - 5 mm large cells. Moreover, the experimentally validated parameter space is highlighted in the stiffness degradation diagram of the I-WP type.

Examining the degradation diagrams, scatter-related fluctuation is observed, especially for stiffness degradation. This is due to the semi-stochastic reconstruction procedure, where the roughness is subject to randomness, cf. Section 2.2. Although this indeterminacy of morphological and mechanical properties allows to capture the process-induced randomness (cf. **Table 5**), scatter in the considered averaged deviation diagrams signifies a convergence error. This issue can be addressed by increasing the number of models per parameter tuple.

In addition to this computational aspect, remarkable mechanical features are shown in **Fig. 14**(a) and (b): generally, the results for the size

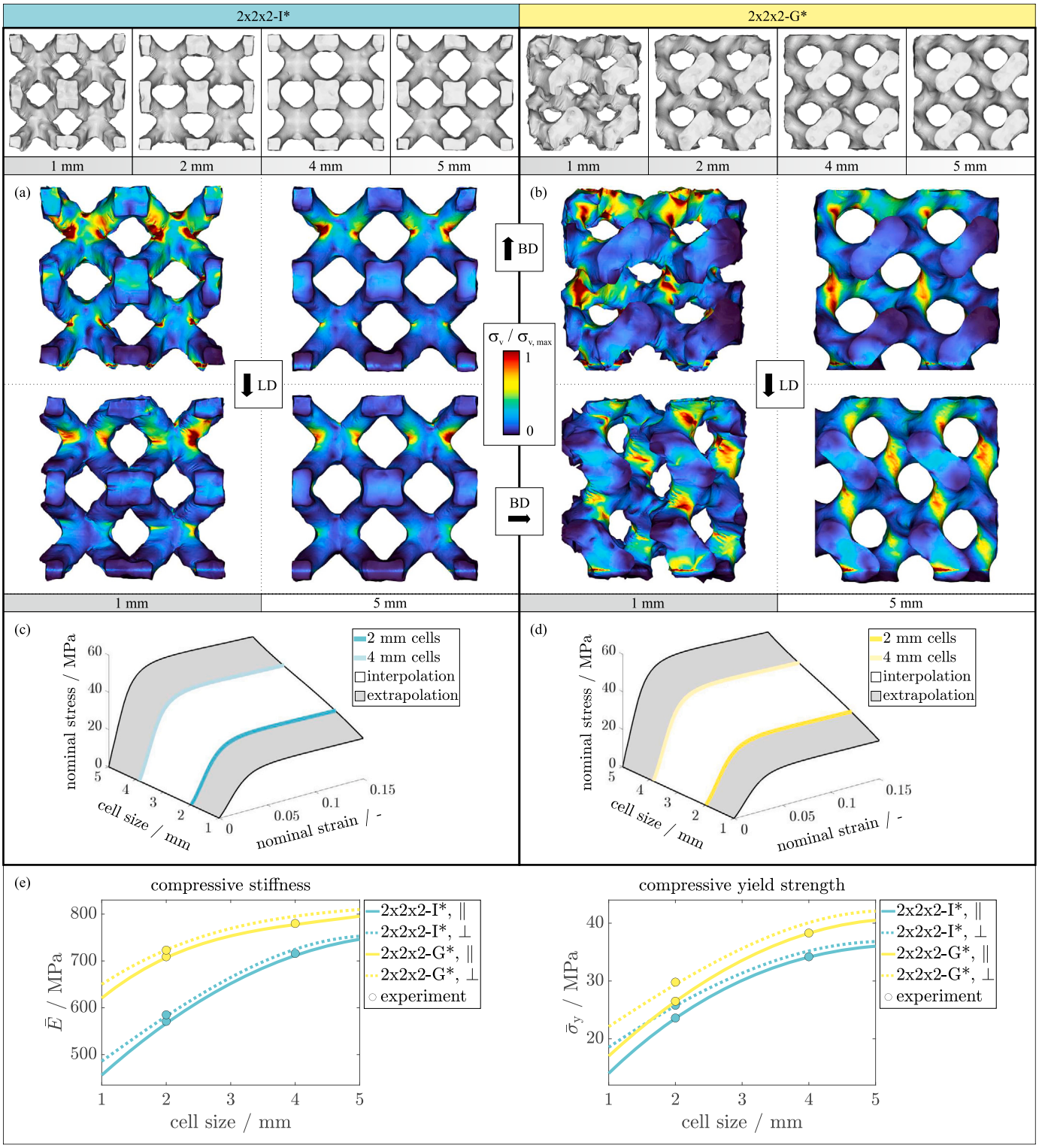

Fig. 13. Effect of cell size on mechanical behavior: in (a) and (b), the von Mises stress distributions for lattices with 1 mm and 5 mm are shown, along with differently sized reconstructions. BD indicates the build direction and LD the load direction. In (c) and (d), the nominal stress-strain curve for the parallel test direction is shown as a function of cell size for modified I-WP and Gyroid lattices. In (e), the compressive effective stiffness $\bar{E}$ and yield strength $\bar{\sigma}_y$ are plotted versus cell size for the parallel (∥) and perpendicular (⊥) test directions.

effect previously discussed in this section prove to be persistent when the parameter space is expanded. Consequently, the larger the amount of imperfections in terms of shift g_1 and g_2 is, the larger is the degradation of stiffness and strength. Although this is true for both TPMS types, the degradation of the I-WP lattice exceeds that of the Gyroid lattice. Specifically, the relative increase in the parameter space considered is about 77% for stiffness and 12% for strength. Thus, not only the morphology of the I-WP lattice proves more predisposed to imperfections, but also its mechanical properties are more defect-sensitive than those of the Gyroid lattice. This robustness to process-related imperfec-

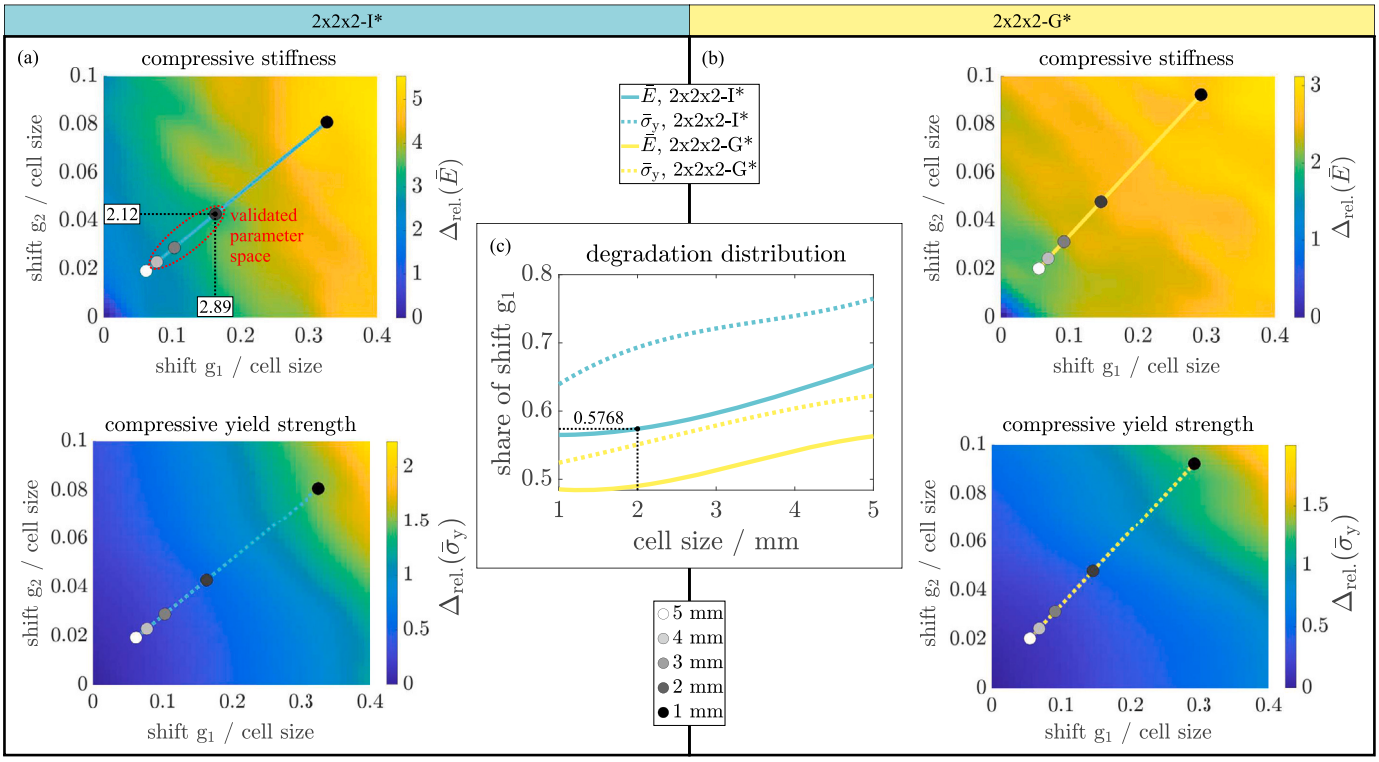

Fig. 14. Mechanical degradation study: in (a) and (b), the degradation of stiffness $\bar{E}$ and strength $\bar{\sigma}_y$ with respect to the as-designed model is shown as a function of shift g_1 for excess material and g_2 for roughness. The plotted lines correspond to the parameter tuples for 1 - 5 mm cell size. In (c), the size-dependent share of g_1 in the degradation is shown. The values marked in black in (a) specify the degradation at the axis intersection points, from which the degradation share is calculated in (c). The validated parameter space is marked in red in (a).

tions may be a key reason for the popularity of the Gyroid TPMS type in research and engineering [17,28]. In addition, stiffness is found to decrease more than strength. Consequently, it can be stated that stiffness is more sensitive to imperfections than strength. Both findings are consistent with the experimental results from Section 3.1 and 3.2.

However, the generalized structure-property relationships performed reveal additional insights. The first observation refers to the topology of the degradation diagrams: while the diagrams of stiffness are dominated by a plateau-like region, those of strength are characterized by a valley-like region. Therefore, a comparatively large stiffness degradation is already present at low shift amounts, cf. the cell sizes of 3 - 5 mm. In contrast, strength decreases appreciably only at larger shifts g_1 and g_2 for cell sizes <2 mm. These features are valuable for BTE: on the one hand, static structural integrity is comparatively little affected by imperfections. On the other hand, stiffness degradation is rather uncritical for implants, where the stress-shielding effect remains a frequent challenge [2,6]. In the context of safety-related applications, another important point is that the reconstructed morphology is always accompanied by a degradation of the mechanical properties. Thus, the proposed simulation approach lends itself as a conservative evaluation tool that reduces the risk of an overly optimistic design.

The second observation arises from the comparison of the g_1- and g_2-sensitivity of the degradation, respectively. Here, the share of mechanical degradation due to shift g_1 seems to be larger than that caused by shift g_2. To examine this in detail, again only the cell size curves are considered and the remaining non-physical part of the diagrams is neglected. For each point, the shares of shift g_1 and g_2 in the degradation are determined using the superposition principle. This is a simplification, since the degradation of the two shifts actually adds up in a nonlinear manner. However, since relative shares are considered here, the resulting error is assumed to be negligible. Furthermore, the assumption of the validity of the superposition principle offers an attractive opportunity: in particular, the degradations caused by the shifts g_1 and g_2 can be read off separately at the axis intersections of the horizontal and vertical perpendiculars, respectively. Doing this for the entire cell size curve yields the share of both imperfection types in the degradation as a function of cell size. The result for stiffness and strength, respectively for I-WP and Gyroid lattice, is shown in **Fig. 14**(c). Here, the share of shift g_1 is shown, but the share of g_2 is implicitly given since both shares add up to 1. As an example of calculation, the stiffness degradation of the I-WP lattice with 2 mm size is illustrated in **Fig. 14**(a) and (c).

Initially, the most important observation in **Fig. 14**(c) concerns the different shares of shifts g_1 and g_2 in the mechanical degradation: for both TPMS types, the share of shift g_1 in the degradation of stiffness and strength exceeds that of g_2. Only the stiffness degradation of the Gyroid lattice with 1 - 2 mm cell size represents a minor exception. Accordingly, excess material on overhanging surfaces appears to be the main driver of mechanical degradation of TPMS lattices. In addition, all degradation distribution curves show a strictly monotonically increasing course. Thus, the larger the cell size is, the more the mechanical behavior depends on the excess material or the shift g_1. Conversely, the smaller the cell size is, the greater is the impact of the surface roughness or shift g_2. The presumed reason for this can be inferred from the stress distributions of the differently sized lattices in **Fig. 13**(a) and (b): above a certain lower limit, no roughness-related influence on the surface stress is evident. Thus, roughness at large cell sizes appears as a subordinate surface phenomenon that hardly affects the stress distribution in the lattice. In contrast, due to its local concentration on overhanging surfaces, shift g_1 is larger than shift g_2. As a result, excess material leads to significant mechanical degradation even at larger cell sizes. This rationale needs to be further substantiated by more in-depth studies in the future.

Moreover, the share of shift g_1 in the degradation is larger for strength than for stiffness, cf. **Fig. 14**(c). Thus, while strength according to **Fig. 13**(e) is generally less sensitive to imperfections, it is particularly sensitive to excess material. This marked dependence of the strength on the excess material applies to both lattice types and to the entire

cell size range considered. However, on closer examination, this phenomenon is more pronounced for the I-WP lattice than for the Gyroid lattice. In fact, the difference for the I-WP lattice with 7.41 - 12.56% is almost twice as large as for the Gyroid lattice with 4.05 - 6.46%. Furthermore, comparison of both TPMSs reveals that the share of shift g_1 in the degradation of both stiffness and strength is lower for the Gyroid than for the I-WP. This finding provides further evidence for the observation from **Fig. 13**(e) that the mechanical degradation of the I-WP lattice exceeds that of the Gyroid lattice.

Accordingly, the insensitivity of Gyroid lattices to imperfections can now be attributed to the less damaging effect of the excess material. Looking at **Fig. 13**(a) and (b), this can be justified by the correlation between defect localization and stress distribution: as noted in Section **3.2**, the excess material is concentrated below the nodes in the I-WP lattice. Since this is a low-stress region during compression, the excess material in the I-WP lattice is mechanically inefficient. In the case of the more uniformly stressed Gyroid lattice, the excess material also affects medium to heavily stressed lattice portions. Consequently, the excess material is more efficient here. The same reasoning can be applied to the second type of imperfection: since roughness is uniformly distributed throughout the lattice, it affects a comparatively large portion of the uniformly stressed Gyroid lattice. In contrast, roughness in the I-WP lattice is predominantly located outside the region of influence of stress peaks. Thus, the roughness-induced degradation of the Gyroid lattice is larger than that of the I-WP lattice.

Finally, predictions of the expected performance gains through LPBF-process optimization and subtractive post-treatments can be derived from the numerical results. On the one hand, process optimization particularly helps to avoid overmelting on overhanging surfaces and thus the formation of excess material. Given the dominant share of shift g_1 in the degradation, process optimization generally promises a greater prospect for performance gains than post-treatments. This applies all the more, the larger the share of shift g_1 is. Accordingly, the cell type I-WP, the mechanical property strength and the large cell sizes are associated with a particularly large potential for process optimization. On the other hand, subtractive post-treatments such as sandblasting [33] and chemical polishing [31] are mainly effective for roughness. Consequently, there is high potential for improvement for the cell type Gyroid, the property strength and the smaller cell sizes.

After analyzing the different degradation shares, the improvement potential can also be predicted independently of the cell type: lattice structures with homogeneous stress distribution are probably more sensitive to roughness and thus subtractive post-treatments. In contrast, heterogeneously stressed structures tend to be more sensitive to excess material or process optimization. Depending on the cell type, size and number, the total improvement potential according to **Table 6** is up to 341% for stiffness and up to 66% for strength. However, the actual extent of the performance gain resulting from process optimization and post-treatment remains open. Another open question concerns the transferability of the results for quasi-static compression behavior to other loading conditions, especially fatigue [17,64]. This is where future work must start in order to validate the numerical results and predictions. For example, valuable information emerges from structure-property studies on post-treated lattices. In particular, subtractive post-treatments allow to investigate the influence of excess material quasi-separately, as they reduce roughness. Promising are also tests on previously unstudied lattice structures, *e.g.*, based on the Schwarz Diamond surface and sheet configuration [65,66]. This helps to assess the generalizability of the methodology.

If these experiments substantiate the validity of the reconstruction procedure, a valuable tool is available for industry and research. On the one hand, the actual morphology of additively manufactured TPMS lattices can be reconstructed for virtual structure-property analysis. This concerns both mechanical behavior and most probably also fluid dynamic properties, such as permeability, which is crucial for osseoconductivity [67,68]. On the other hand, arbitrary imperfect states of a lattice can be modeled to predict the structural properties. This helps to define defect tolerances non-destructively and to decide on the advisability of process optimization and post-treatment. This option is particularly attractive for industrial use, as it promotes the digitization of product development. Here, another advantage is that the as-built morphology is artificially reconstructed instead of relying on a one-to-one copy of the µ-CT data. Thus, after the modeling parameters are determined experimentally, the procedure does not require high-quality instrumentation. This is crucial since µ-CT data are often not available in practice due to component dimensions and effort.

4. Conclusion

The structure-property relationships of eight promising bone substitutes based on triply periodic minimal surfaces (TPMS) made of laser powder bed fused (LPBF) Ti-42Nb were investigated. Experimentally, firstly, the imperfect lattice morphology was examined using µ-CT scans before uniaxial compression tests were performed. Numerical work focused on reconstructing the as-built morphology, including process-related features such as roughness and excess material on overhanging surfaces. Further simulations were conducted to explore the mechanical size effect as well as the degradation shares of the different defect types. The following conclusions can be drawn:

- In the as-built state, LPBF processed TPMS lattices feature external imperfections, the extent of which depends sensitively on the lattice type and cell size. Due to the larger surface fraction with overhang exceeding 45°, the I-WP lattice tends to have larger target-actual deviations than the Gyroid lattice. Moreover, the deviations are larger for 2 mm cell size than for 4 mm, which is attributed to the smaller material volume and poorer heat dissipation.
- The presented modeling procedure enables the reconstruction of the external as-built morphology of TPMS lattices. Here, the relative Boolean difference volume Δ_{BOOL} with respect to the µ-CT data proves to be a suitable descriptor of the reconstruction quality. Specifically, the reconstructed models exhibit only about 50% relative Boolean difference volume Δ_{BOOL} compared to the idealized as-design models.
- In uniaxial compression tests, I-WP and Gyroid lattices show excellent suitability for implant applications given high ductility, low stiffness to below 1 GPa and high yield strength to above 35 MPa. However, morphological imperfections prove to be a formative factor for the resulting stiffness and strength. Here, the larger the relative target-actual deviation is, the more the structural integrity is impaired. In addition, the characteristic values of the lattices are lower when tests are performed parallel to the building direction compared to perpendicular test direction.
- Performing finite element simulations reveals that the experimentally measured compressive behavior is drastically overestimated by the as-designed models. In particular, the overestimation of stiffness is up to 341% and that of yield strength is up to 66%. In contrast, the deviations for the reconstructed models are much smaller, with a maximum deviation of 26% for stiffness and 12% for strength.
- Numerical investigations on the defect-related size effect show that compressive stiffness and strength increase degressively with cell size. Further simulations indicate that the share of excess material in mechanical degradation is larger than that of roughness. This is especially true for yield strength and lattices with larger cell sizes. Furthermore, the share of excess material in degradation is larger for the I-WP lattices than for the Gyroids, which is ascribed to the larger proportion of overhanging surfaces [50].

The results encourage to use the presented methodology for further structure-property investigations. On the one hand, future work aims at minimizing the morphological target-actual deviation. For this pur-

pose, LPBF process optimizations are performed by targeted parameter modulation as well as post-treatment processes such as chemical polishing and annealing. On the other hand, the reconstruction procedure is modified by introducing directional surface roughness. This is intended to more accurately represent the actual as-built morphology. Finally, other structure-property relationships such as fatigue strength and permeability of imperfect lattices are explored. If these studies confirm the general procedure, a data-driven design tool is available that greatly facilitates the use of TPMS lattices for both research and industry.

Declaration of competing interest

The authors declare that they have no known competing financial interests or personal relationships that could have appeared to influence the work reported in this paper.

Data availability

Data will be made available on request.

Funding

The authors gratefully acknowledge funding from the German Research Foundation (DFG) within the framework of the research projects ZI 1006/16-2 and GE/1106/12-2 (No. 419952351).

Acknowledgements

The authors are grateful to S. Schettler, P. Lepper and R. Rao for their assistance with the experimental work. Furthermore, the support of U. Kühn with respect to fruitful scientific discussions is acknowledged.

References

[1] N. Soro, N. Saintier, J. Merzeau, M. Veidt, M.S. Dargusch, Quasi-static and fatigue properties of graded ti–6al–4v lattices produced by laser powder bed fusion (lpbf), Addit. Manuf. 37 (2021) 101653, https://doi.org/10.1016/j.addma.2020.101653.

[2] C. Torres-Sanchez, F. Al Mushref, M. Norrito, K. Yendall, Y. Liu, P. Conway, The effect of pore size and porosity on mechanical properties and biological response of porous titanium scaffolds, Mater. Sci. Eng., C, Biomim. Mater., Sens. Syst. 77 (2017) 219–228, https://doi.org/10.1016/j.msec.2017.03.249, https://www.sciencedirect.com/science/article/pii/S092849311632793X.

[3] J. Feng, J. Fu, X. Yao, Y. He, Triply periodic minimal surface (tpms) porous structures: from multi-scale design, precise additive manufacturing to multidisciplinary applications, Int. J. Extrem. Manuf. 4 (2) (2022) 022001, https://doi.org/10.1088/2631-7990/ac5be6.

[4] N. Kladovasilakis, K. Tsongas, D. Tzetzis, Finite element analysis of orthopedic hip implant with functionally graded bioinspired lattice structures, Biomimetics 5 (3) (2020) 44, https://doi.org/10.3390/biomimetics5030044.

[5] S.C. Kapfer, S.T. Hyde, K. Mecke, C.H. Arns, G.E. Schröder-Turk, Minimal surface scaffold designs for tissue engineering, Biomaterials 32 (29) (2011) 6875–6882, https://doi.org/10.1016/j.biomaterials.2011.06.012.

[6] T. Poltue, C. Karuna, S. Khrueaduangkham, S. Seehanam, P. Promoppatum, Design exploration of 3d-printed triply periodic minimal surface scaffolds for bone implants, Int. J. Mech. Sci. 211 (2021) 106762, https://doi.org/10.1016/j.ijmecsci.2021.106762.

[7] R. Asbai-Ghoudan, S.R. de Galarreta, N. Rodriguez-Florez, Analytical model for the prediction of permeability of triply periodic minimal surfaces, J. Mech. Behav. Biomed. Mater. (2021) 104804, https://doi.org/10.1016/j.jmbbm.2021.104804.

[8] X.-Y. Zhang, X.-C. Yan, G. Fang, M. Liu, Biomechanical influence of structural variation strategies on functionally graded scaffolds constructed with triply periodic minimal surface, Addit. Manuf. 32 (2020) 101015, https://doi.org/10.1016/j.addma.2019.101015.

[9] O. Al-Ketan, R.K. Abu, Al-Rub, Mslattice: a free software for generating uniform and graded lattices based on triply periodic minimal surfaces, Mat. Design Process. Comm. 3 (6) (2021) e205, https://doi.org/10.1002/mdp2.205.

[10] J. Deering, K. Grandfield, Current interpretations on the in vivo response of bone to additively manufactured metallic porous scaffolds: a review, Biomater. Biosyst. 2 (2021) 100013, https://doi.org/10.1016/j.bbiosy.2021.100013.

[11] M.A. Khorshidi, Length scale parameter of single trabecula in cancellous bone, Biomech. Model. Mechanobiol. 19 (5) (2020) 1917–1923, https://doi.org/10.1007/s10237-020-01316-5.

[12] Y. Zheng, Q. Han, D. Li, F. Sheng, Z. Song, J. Wang, Promotion of tendon growth into implant through pore-size design of a ti-6al-4 v porous scaffold prepared by 3d printing, Mater. Des. 197 (2021) 109219, https://doi.org/10.1016/j.matdes.2020.109219.

[13] Y. Xiong, W. Wang, R. Gao, H. Zhang, L. Dong, J. Qin, B. Wang, W. Jia, X. Li, Fatigue behavior and osseointegration of porous ti-6al-4v scaffolds with dense core for dental application, Mater. Des. 195 (2020) 108994, https://doi.org/10.1016/j.matdes.2020.108994.

[14] S. Pilz, T. Gustmann, F. Günther, M. Zimmermann, U. Kühn, A. Gebert, Controlling the Young's modulus of a ß-type ti-nb alloy via strong texturing by lpbf, Mater. Des. 216 (2022) 110516, https://doi.org/10.1016/j.matdes.2022.110516.

[15] D. Ali, M. Ozalp, S.B. Blanquer, S. Onel, Permeability and fluid flow-induced wall shear stress in bone scaffolds with tpms and lattice architectures: a cfd analysis, Eur. J. Mech. B, Fluids 79 (2020) 376–385, https://doi.org/10.1016/j.euromechflu.2019.09.015.

[16] J.M. García-Aznar, G. Nasello, S. Hervas-Raluy, M.Á. Pérez, M.J. Gómez-Benito, Multiscale modeling of bone tissue mechanobiology, Bone (2021) 116032, https://doi.org/10.1016/j.bone.2021.116032.

[17] M. Benedetti, A. Du Plessis, R. Ritchie, M. Dallago, S. Razavi, F. Berto, Architected cellular materials: a review on their mechanical properties towards fatigue-tolerant design and fabrication, Mater. Sci. Eng., R Rep. 144 (2021) 100606, https://doi.org/10.1016/j.mser.2021.100606.

[18] B. Blakey-Milner, P. Gradl, G. Snedden, M. Brooks, J. Pitot, E. Lopez, M. Leary, F. Berto, A. du Plessis, Metal additive manufacturing in aerospace: a review, Mater. Des. 209 (2021) 110008, https://doi.org/10.1016/j.matdes.2021.110008.

[19] A. Jones, M. Leary, S. Bateman, M. Easton, Parametric design and evaluation of tpms-like cellular solids, Mater. Des. 221 (2022) 110908, https://doi.org/10.1016/j.matdes.2022.110908.

[20] C. Pan, Y. Han, J. Lu, Design and optimization of lattice structures: a review, Appl. Sci. 10 (18) (2020) 6374, https://doi.org/10.3390/app10186374.

[21] K. Yeranee, Y. Rao, A review of recent investigations on flow and heat transfer enhancement in cooling channels embedded with triply periodic minimal surfaces (tpms), Energies 15 (23) (2022) 8994, https://doi.org/10.3390/app10186374.

[22] L. Li, J. Shi, K. Zhang, L. Yang, F. Yu, L. Zhu, H. Liang, X. Wang, Q. Jiang, Early osteointegration evaluation of porous ti6al4v scaffolds designed based on triply periodic minimal surface models, J. Orthop. Trans. 19 (2019) 94–105, https://doi.org/10.1016/j.jot.2019.03.003.

[23] B. Charbonnier, M. Manassero, M. Bourguignon, A. Decambron, H. El-Hafci, C. Morin, D. Leon, M. Bensidoum, S. Corsia, H. Petite, et al., Custom-made macroporous bioceramic implants based on triply-periodic minimal surfaces for bone defects in load-bearing sites, Acta Biomater. 109 (2020) 254–266, https://doi.org/10.1016/j.actbio.2020.03.016.

[24] C.N. Kelly, T. Wang, J. Crowley, D. Wills, M.H. Pelletier, E.R. Westrick, S.B. Adams, K. Gall, W.R. Walsh, High-strength, porous additively manufactured implants with optimized mechanical osseointegration, Biomaterials 279 (2021) 121206, https://doi.org/10.1016/j.biomaterials.2021.121206.

[25] M. Dziaduszewska, A. Zieliński, Structural and material determinants influencing the behavior of porous ti and its alloys made by additive manufacturing techniques for biomedical applications, Materials 14 (4) (2021) 712, https://doi.org/10.3390/ma14040712.

[26] I. Echeta, X. Feng, B. Dutton, R. Leach, S. Piano, Review of defects in lattice structures manufactured by powder bed fusion, Int. J. Adv. Manuf. Technol. 106 (5) (2020) 2649–2668, https://doi.org/10.1007/s00170-019-04753-4.

[27] A. Du Plessis, S.M.J. Razavi, F. Berto, The effects of microporosity in struts of gyroid lattice structures produced by laser powder bed fusion, Mater. Des. 194 (2020) 108899, https://doi.org/10.1016/j.matdes.2020.108899.

[28] O. Al-Ketan, R.K. Abu, Al-Rub, multifunctional mechanical metamaterials based on triply periodic minimal surface lattices, Adv. Eng. Mater. 21 (10) (2019) 1900524, https://doi.org/10.1002/adem.201900524.

[29] M. Tang, P.C. Pistorius, J.L. Beuth, Prediction of lack-of-fusion porosity for powder bed fusion, Addit. Manuf. 14 (2017) 39–48, https://doi.org/10.1016/j.addma.2016.12.001.

[30] Z. Alomar, F. Concli, A review of the selective laser melting lattice structures and their numerical models, Adv. Eng. Mater. 22 (12) (2020) 2000611, https://doi.org/10.1002/adem.202000611.

[31] A.K. Singla, M. Banerjee, A. Sharma, J. Singh, A. Bansal, M.K. Gupta, N. Khanna, A. Shahi, D.K. Goyal, Selective laser melting of ti6al4v alloy: process parameters, defects and post-treatments, J. Manuf. Process. 64 (2021) 161–187, https://doi.org/10.1016/j.jmapro.2021.01.009.

[32] L. Yang, C. Yan, Z. Liu, B. Song, S. Wen, C. Zhang, Y. Shi, S. Yang, Compression–compression fatigue behaviour of gyroid-type triply periodic minimal surface porous structures fabricated by selective laser melting, Acta Mater. 181 (2019) 49–66, https://doi.org/10.1016/j.actamat.2019.09.042.

[33] A. Ataee, Y. Li, D. Fraser, G. Song, C. Wen, Anisotropic ti-6al-4v gyroid scaffolds manufactured by electron beam melting (ebm) for bone implant applications, Mater. Des. 137 (2018) 345–354, https://doi.org/10.1016/j.matdes.2017.10.040.

[34] E. Davoodi, H. Montazerian, R. Esmaeilizadeh, A.C. Darabi, A. Rashidi, J. Kadkhodapour, H. Jahed, M. Hoorfar, A.S. Milani, P.S. Weiss, et al., Additively manufactured gradient porous ti–6al–4v hip replacement implants embedded with cell-laden gelatin methacryloyl hydrogels, ACS Appl. Mater. Interfaces 13 (19) (2021) 22110–22123, https://doi.org/10.1021/acsami.0c20751.

[35] S. Zou, Y. Mu, B. Pan, G. Li, L. Shao, J. Du, Y. Jin, Mechanical and biological properties of enhanced porous scaffolds based on triply periodic minimal surfaces, Mater. Des. (2022) 110803, https://doi.org/10.1016/j.matdes.2022.110803.
[36] J. Zhang, Y. Shen, Y. Sun, J. Yang, Y. Gong, K. Wang, Z. Zhang, X. Chen, L. Bai, Design and mechanical testing of porous lattice structure with independent adjustment of pore size and porosity for bone implant, J. Mater. Res. Technol. 18 (2022) 3240–3255, https://doi.org/10.1016/j.jmrt.2022.04.002.
[37] L. Yang, M. Ferrucci, R. Mertens, W. Dewulf, C. Yan, Y. Shi, S. Yang, An investigation into the effect of gradients on the manufacturing fidelity of triply periodic minimal surface structures with graded density fabricated by selective laser melting, J. Mater. Process. Technol. 275 (2020) 116367, https://doi.org/10.1016/j.jmatprotec.2019.116367.
[38] S. Liu, Y.C. Shin, Additive manufacturing of ti6al4v alloy: a review, Mater. Des. 164 (2019) 107552, https://doi.org/10.1016/j.matdes.2018.107552.
[39] T. Maconachie, M. Leary, B. Lozanovski, M. Brandt, Slm lattice structures: properties, performance, applications and challenges, Mater. Des. 183 (2019) 108137, https://doi.org/10.1016/j.matdes.2019.108137.
[40] L. Zhang, S. Feih, S. Daynes, S. Chang, M.Y. Wang, J. Wei, W.F. Lu, Energy absorption characteristics of metallic triply periodic minimal surface sheet structures under compressive loading, Addit. Manuf. 23 (2018) 505–515, https://doi.org/10.1016/j.addma.2018.08.007.
[41] U. Gebhardt, T. Gustmann, L. Giebeler, F. Hirsch, J.K. Hufenbach, M. Kästner, Additively manufactured alsi10mg lattices – potential and limits of modelling as-designed structures, Mater. Des. (2022) 110796, https://doi.org/10.1016/j.matdes.2022.110796.
[42] H.A. Zaharin, A.M. Abdul Rani, F.I. Azam, T.L. Ginta, N. Sallih, A. Ahmad, N.A. Yunus, T.Z.A. Zulkifli, Effect of unit cell type and pore size on porosity and mechanical behavior of additively manufactured ti6al4v scaffolds, Materials 11 (12) (2018) 2402, https://doi.org/10.3390/ma11122402.
[43] L. Liu, P. Kamm, F. García-Moreno, J. Banhart, D. Pasini, Elastic and failure response of imperfect three-dimensional metallic lattices: the role of geometric defects induced by selective laser melting, J. Mech. Phys. Solids 107 (2017) 160–184, https://doi.org/10.1016/j.jmps.2017.07.003.
[44] Y. Amani, S. Dancette, P. Delroisse, A. Simar, E. Maire, Compression behavior of lattice structures produced by selective laser melting: X-ray tomography based experimental and finite element approaches, Acta Mater. 159 (2018) 395–407, https://doi.org/10.1016/j.actamat.2018.08.030.
[45] M. Dallago, F. Zanini, S. Carmignato, D. Pasini, M. Benedetti, Effect of the geometrical defectiveness on the mechanical properties of slm biomedical ti6al4v lattices, Proc. Struct. Integrity 13 (2018) 161–167, https://doi.org/10.1016/j.prostr.2018.12.027.
[46] M. Dallago, B. Winiarski, F. Zanini, S. Carmignato, M. Benedetti, On the effect of geometrical imperfections and defects on the fatigue strength of cellular lattice structures additively manufactured via selective laser melting, Int. J. Fatigue 124 (2019) 348–360, https://doi.org/10.1016/j.ijfatigue.2019.03.019.
[47] B. Lozanovski, M. Leary, D. Shidid, M. Qian, M. Brandt, Computational modelling of strut defects in slm manufactured lattice structures, Mater. Des. 171 (2019) 107671, https://doi.org/10.1016/j.matdes.2019.107671.
[48] B. Lozanovski, D. Downing, A. du Plessis, P. Tran, J. Jakeman, D. Shidid, C. Emmelmann, M. Qian, P. Choong, et al., Non-destructive simulation of node defects in additively manufactured lattice structures, Addit. Manuf. 36 (2020) 101593, https://doi.org/10.1016/j.addma.2020.101593.
[49] T. Maconachie, R. Tino, B. Lozanovski, M. Watson, A. Jones, C. Pandelidi, A. Alghamdi, A. Almalki, D. Downing, M. Brandt, et al., The compressive behaviour of abs gyroid lattice structures manufactured by fused deposition modelling, Int. J. Adv. Manuf. Technol. 107 (11) (2020) 4449–4467, https://doi.org/10.1007/s00170-020-05239-4.
[50] F. Günther, F. Hirsch, S. Pilz, M. Wagner, A. Gebert, M. Kästner, M. Zimmermann, Structure-property relationships of imperfect additively manufactured lattices based on triply periodic minimal surfaces, Mater. Des. (2022) 111036, https://doi.org/10.1016/j.matdes.2022.111036.
[51] F. Günther, M. Wagner, S. Pilz, A. Gebert, M. Zimmermann, Design procedure for triply periodic minimal surface based biomimetic scaffolds, J. Mech. Behav. Biomed. Mater. 126 (2022) 104871, https://doi.org/10.1016/j.jmbbm.2021.104871.
[52] F. Günther, S. Pilz, F. Hirsch, M. Wagner, M. Kästner, A. Gebert, M. Zimmermann, Shape optimization of additively manufactured lattices based on triply periodic minimal surfaces, Addit. Manuf. (2023) 103659, https://doi.org/10.1016/j.addma.2023.103659.
[53] R. Raghava, R.M. Caddell, G.S. Yeh, The macroscopic yield behaviour of polymers, J. Mater. Sci. 8 (2) (1973) 225–232, https://doi.org/10.1007/BF00550671.
[54] A. Ataee, M. Brandt, C. Wen, Ultrahigh-strength titanium gyroid scaffolds manufactured by selective laser melting (slm) for bone implant applications, Acta Mater. 158 (2018) 354–368, https://doi.org/10.1016/j.actamat.2018.08.005.
[55] Z. Liu, H. Gong, J. Gao, Enhancement in the fatigue resistances of triply periodic surfaces-based scaffolds, Int. J. Mech. Sci. (2023) 108119, https://doi.org/10.1016/j.ijmecsci.2023.108119.
[56] C. Zhang, H. Zheng, L. Yang, Y. Li, J. Jin, W. Cao, C. Yan, Y. Shi, Mechanical responses of sheet-based gyroid-type triply periodic minimal surface lattice structures fabricated using selective laser melting, Mater. Des. 214 (2022) 110407, https://doi.org/10.1016/j.matdes.2022.110407.
[57] J. Fu, J. Ding, S. Qu, L. Zhang, M.Y. Wang, M. Fu, X. Song, Improved light-weighting potential of ss316l triply periodic minimal surface shell lattices by micro laser powder bed fusion, Mater. Des. 222 (2022) 111018, https://doi.org/10.1016/j.matdes.2022.111018.
[58] E. Vermesse, C. Mabru, L. Arurault, Surface integrity after pickling and anodization of ti–6al–4v titanium alloy, Appl. Surf. Sci. 285 (2013) 629–637, https://doi.org/10.1016/j.apsusc.2013.08.103.
[59] Z. Cai, Z. Liu, X. Hu, H. Kuang, J. Zhai, The effect of porosity on the mechanical properties of 3d-printed triply periodic minimal surface (tpms) bioscaffold, Bio-Des. Manuf. 2 (4) (2019) 242–255, https://doi.org/10.1007/s42242-019-00054-7.
[60] J.H. Peck, K.D. Kavlock, B.M. Ferrell, D.G. Peck, A.E. Dmitriev, Mechanical performance of lumbar intervertebral body fusion devices: an analysis of data submitted to the food and drug administration, J. Biomech. 78 (2018) 87–93, https://doi.org/10.1016/j.jbiomech.2018.07.022.
[61] W. Radlof, C. Benz, M. Sander, Numerical and experimental investigations of additively manufactured lattice structures under quasi-static compression loading, Mat. Design Process. Comm. 3 (3) (2021) e164, https://doi.org/10.1002/mdp2.164.
[62] X. Yang, Q. Yang, Y. Shi, L. Yang, S. Wu, C. Yan, Y. Shi, Effect of volume fraction and unit cell size on manufacturability and compressive behaviors of ni-ti triply periodic minimal surface lattices, Addit. Manuf. 54 (2022) 102737, https://doi.org/10.1016/j.addma.2022.102737.
[63] D. Barba, E. Alabort, R. Reed, Synthetic bone: design by additive manufacturing, Acta Biomater. 97 (2019) 637–656, https://doi.org/10.1016/j.actbio.2019.07.049.
[64] F. Bobbert, K. Lietaert, A.A. Eftekhari, B. Pouran, S. Ahmadi, H. Weinans, A. Zadpoor, Additively manufactured metallic porous biomaterials based on minimal surfaces: a unique combination of topological, mechanical, and mass transport properties, Acta Biomater. 53 (2017) 572–584, https://doi.org/10.1016/j.actbio.2017.02.024.
[65] O. Al-Ketan, M. Pelanconi, A. Ortona, R.K. Abu Al-Rub, Additive manufacturing of architected catalytic ceramic substrates based on triply periodic minimal surfaces, J. Am. Ceram. Soc. 102 (10) (2019) 6176–6193, https://doi.org/10.1111/jace.16474.
[66] S. Vijayavenkataraman, J.Y. Hsi Fuh, W.F. Lu, Triply periodic minimal surfaces sheet scaffolds for tissue engineering applications: an optimization approach toward biomimetic scaffold design, ACS Appl. Bio Mater. 1 (2) (2018) 259–269, https://doi.org/10.1021/acsabm.8b00052.
[67] S. Ma, Q. Tang, X. Han, R. Setchi, Y. Liu, Y. Liu, A. Goulas, D.S. Engstrøm, et al., Manufacturability, mechanical properties, mass-transport properties and biocompatibility of triply periodic minimal surface (tpms) porous scaffolds fabricated by selective laser melting, Mater. Des. 195 (2020) 109034, https://doi.org/10.1016/j.matdes.2020.109034.
[68] G. Yu, Z. Li, S. Li, Y. Hua, H. Liu, X. Zhao, D.T. Dhaidhai, W. Li, X. Wang, The select of internal architecture for porous ti alloy scaffold: a compromise between mechanical properties and permeability, Mater. Des. 192 (2020) 108754.